

COHERENT STRUCTURES AT ION SCALES IN FAST SOLAR WIND: *CLUSTER* OBSERVATIONS

D. PERRONE¹, O. ALEXANDROVA², O. W. ROBERTS³, S. LION², C. LACOMBE², A. WALSH¹, M. MAKSIMOVIC², I. ZOUGANELIS¹

¹ European Space Agency, ESAC, Madrid, Spain.

² LESIA, Observatoire de Paris, PSL Research University, CNRS, Sorbonne Universits, UPMC Univ. Paris 06, Univ. Paris Diderot, Sorbonne Paris Cité, France.

³ European Space Agency, ESTEC, Noordwijk, Netherlands.

Draft version March 13, 2022

ABSTRACT

We investigate the nature of magnetic turbulent fluctuations, around ion characteristic scales, in a fast solar wind stream, by using *Cluster* data. Contrarily to slow solar wind, where both Alfvénic ($\delta b_{\perp} \gg \delta b_{\parallel}$) and compressive ($\delta b_{\parallel} \gg \delta b_{\perp}$) coherent structures are observed (Perrone et al. 2016), the turbulent cascade of fast solar wind is dominated by Alfvénic structures, namely Alfvén vortices, with small and/or finite compressive part, with the presence also of several current sheets aligned with the local magnetic field. Several examples of vortex chains are also recognized. Although an increase of magnetic compressibility around ion scales is observed also for fast solar wind, no strongly compressive structures are found, meaning that the nature of the slow and fast winds is intrinsically different. Multi-spacecraft analysis applied to this interval of fast wind indicate that the coherent structures are almost convected by the flow and aligned with the local magnetic field, i.e. their normal is perpendicular to \mathbf{B} , that is consistent with a two dimensional turbulence picture. Understanding intermittency and the related generation of coherent structures could provide a key insight into the nonlinear energy transfer and dissipation processes in magnetized and collisionless plasmas.

1. INTRODUCTION

Turbulence is a complex, fascinating and highly non-linear process ubiquitous in nature. The dynamical evolution of a turbulent system is a consequence of the non-linearity responsible for the coupling of many degrees of freedom, which leads the system far from thermal equilibrium. In typical hydrodynamic systems, the energy, injected at large scales, is transferred self-consistently towards smaller scales, where it finally can be dissipated (Kolmogorov 1941). Moreover, the turbulent activity becomes more and more inhomogeneous and non-uniform as the energy arrives to smaller and smaller scales. This phenomenon, named intermittency (Frisch 1995), is due to the presence of coherent structures, i.e. filaments of the vorticity field localized in space but covering scales from about the integral scale to the dissipation scale and with a characteristic tube-like structure (She et al. 1990; Frisch 1995). These intermittent events contain most of the energy of the flow. Although for classical fluids the turbulence is fairly well understood, in plasma physics this process represents one of the most spectacular and unsolved problems, where both cross-scale couplings and kinetic effects are present. In this case, indeed, the energy, injected at large scales, progressively decays towards smaller scales, where kinetic effects (heating, particle acceleration and so on) dominate the plasma dynamics.

Thanks to the support of many space missions, we have the unique opportunity to analyze directly the dynamics of a natural turbulent plasma: the solar wind, a continuous, but highly variable, weakly collisional and multi-component plasma outflow from the Sun that travels at high speed. ‘In situ’ measurements generally show that the interplanetary medium is in a state of fully developed turbulence, characterized by a multi-scale nonlinear be-

havior (Bruno & Carbone 2013). In the inertial range the turbulent magnetic field cascade manifests a power law similar to the fluid behavior (Kolmogorov 1941). However, around ion characteristic scales, a change in the spectral shape is observed, with the presence of a steeper spectrum (Leamon et al. 1998, 2000; Bale et al. 2005; Smith et al. 2006; Alexandrova et al. 2007, 2008; Bourouaine et al. 2012; Bruno et al. 2014; Lion et al. 2016) and an increase of the magnetic compressibility (Alexandrova et al. 2007, 2008; Hamilton et al. 2008; Salem et al. 2012; Kiyani et al. 2013; Telloni et al. 2015; Lacombe et al. in press). In this frequency range, often called dissipation range, the plasma dynamics is governed by kinetic effects, namely strong anisotropies in the ion velocity distributions, with preferential perpendicular heating and parallel accelerated particles with respect to the background magnetic field. At scales smaller than the ion characteristic scales and up to a fraction of the characteristic electron lengths, another general spectrum is observed, whose interpretation is still controversial (Alexandrova et al. 2009, 2012; Sahraoui et al. 2010, 2013).

A very important aspect of the solar wind turbulent cascade is intermittency, due to the non-Gaussian and bursty nature of the turbulent fluctuations, with the non-Gaussianity that increases towards smaller scales. Therefore, as in the fluid case, also in the solar wind the energy is not uniformly distributed in space (Bruno et al. 2001), but is localized in coherent structures, i.e. structures characterized by a phase synchronization among a certain number of scales. A clear link exists between intermittency, non-Gaussianity and phase coherence. Koga et al. (2007) have shown, in the solar wind turbulence near the Earth’s bow shock, that exists a similar behavior between the phase coherence index and the

kurtosis (flatness), reflecting a departure from Gaussianity of the probability density function of the magnetic field fluctuations, where the non-Gaussianity of the fluctuations is a clear signature of intermittency.

During the last decades, the presence of planar structures, such as current sheets, rotational discontinuities and shocks (Veltri & Mangeney 1999; Veltri 1999; Salem et al. 2009; Greco et al. 2012a; Perri et al. 2012; Greco & Perri 2014), was considered to be the principal cause of intermittency in solar wind at ion scales. Recent studies have shown that other types of coherent structures also contribute to the intermittency phenomenon in the solar wind turbulence. Lion et al. (2016) have shown the presence of Alfvén vortex-like structures in a fast solar wind stream by using *Wind* measurements. Moreover, a study by Roberts et al. (2016) using multi-satellite measurement from *Cluster* spacecraft has shown a well-defined Alfvén vortex in a slow solar wind stream. These structures occur close to ion characteristic scales, similar to what happens to the vortices observed in the Earth’s and Saturn’s magnetosheaths (Alexandrova et al. 2006; Alexandrova & Saur 2008).

More recently, a statistical analysis of coherent structures around ion scales in a slow solar wind stream has been performed by Perrone et al. (2016), using *Cluster* measurements. This study has shown, for the first time, that different families of coherent structures participate to the intermittency at ion scales in slow solar wind, such as compressive structures, i.e. magnetic holes, solitons and shocks; and alfvénic structures in form of current sheets and vortices. These last ones can have an important compressive part and they are the most frequently observed during the analyzed interval. All the observed structures are field aligned with normals perpendicular to the local mean magnetic field, that is consistent with two dimensional ($k_{\perp} \gg k_{\parallel}$) turbulence. Moreover, although most of the structures are merely advected by the wind, the 25% of the analyzed structures propagate in the plasma reference frame.

Despite the fact that several studies have been performed to understand the complex behavior of the solar wind, the nature of the turbulent fluctuations around ion scales and the dissipation in such collisionless medium still remain an open question. The purpose of the present paper is to shed light on the nature of the turbulent fluctuations around ion scales in fast solar wind by using multi-point measurements from *Cluster* spacecraft. The fast solar wind is generally characterized by a higher proton temperature and a lower density with respect to the slow solar wind. Other differences between the two streams are the composition, the Alfvénic content and the anisotropies in ion and electron temperatures.

In the present work, first we focus on the turbulent character of the considered stream and on the phase coherence between the components of the magnetic field, by using wavelet analysis (Farge 1992; Torrence & Compo 1998). Wavelet transforms are a mathematical method, which allow unfolding a signal, or a field, into both time and scale at once. The wavelet analysis can be performed locally on the signal, as opposed to the Fourier transform, which is inherently nonlocal. By expanding the signal in a set of functions that are localized in time as well as in frequency, it is possible to highlight the presence of regions characterized by intermittency in the consid-

ered stream, thus studying the ‘texture’ of the turbulence. Then, we investigate in detail the magnetic field fluctuations close to the ion scales by using the *timing* method for the analysis of multi-satellite data (Schwartz 1998; Perrone et al. 2016). The considered interval of solar wind appears to be characterized by the presence of coherent structures. Moreover, by applying the *multi-point signal resonator* technique (Narita et al. 2011a,b) to the same magnetic fluctuations, we verify the applicability of the *k-filtering* in the case of strong turbulence, i.e. in the presence of coherent structures.

Finally, as a result of the statistical studies on the coherent structures observed in the stream, we find that the ion scales are dominated by Alfvén vortices, with small and/or finite compressive part. Moreover, we observe the presence also of several current sheets aligned with the magnetic field, almost convected by the wind. The comparison of these results with the results presented in Perrone et al. (2016) suggests that the physics that governs the ion scales of fast and slow solar wind is quite different.

The paper is organized as follows: in Section 2 we describe the selected data interval of fast solar wind in terms of plasma parameters and turbulent behavior; and in Section 3 we discuss the concepts of intermittency and phase coherence. In Section 4 we present some examples of detected coherent structures and theoretical models in order to explain the observations. In Section 5 we determine spatial orientation and plasma frame velocities of the observed structures by using multi-satellite analysis; and, in Section 6 we summarize the results and we discuss our conclusions. Finally, in the Appendix, we present the results of the *multi-point signal resonator* technique.

2. FAST SOLAR WIND INTERVAL

We consider an interval of about 40 minutes (17:30-18:10 UT) of undisturbed solar wind from *Cluster* spacecraft on 2004 January 31st. It is a stream of fast solar wind, with a mean speed of about 600 km/s, characterized by a mean magnetic field of about 8.3 nT, a mean proton density of about 3-4 cm^{-3} , and a mean proton temperature of about ~ 37 eV, with $T_{\parallel,p} \sim 30$ eV and $T_{\perp,p} \sim 41$ eV. In terms of characteristic plasma scales, the proton Larmor radius, defined as the ratio between the perpendicular proton thermal speed and the proton cyclotron frequency, is $\rho_p \sim 109$ km; while the proton inertial length, defined as the ratio between the light speed and the proton plasma frequency, is $\lambda_p \sim 121$ km. Finally, the proton plasma beta, β_p , defined as the ratio between the proton kinetic pressure and magnetic pressure, has an averaged value in the interval of about 0.8, with several regions where $\beta_p > 1$.

Although some caveats exist for the electron moments by using the Plasma Electron and Current Experiment (PEACE) (Johnstone et al. 1997; Fazakerley et al. 2009) in this interval of fast solar wind, the mean parallel and perpendicular temperatures are about $T_{\parallel,e} \sim 18$ eV and $T_{\perp,e} \sim 14$ eV, respectively. Therefore, the electron Larmor radius is $\rho_e \sim 1.5$ km. By using the Waves of High Frequency and Sounder for Probing of the Electron Density by Relaxation (WHISPER) experiment (Décréau et al. 2001), the electron density is known ($\sim 4 \text{ cm}^{-3}$) with a resolution of 1.5 s and the electron inertial length can be derived ($\lambda_e \sim 2.6$ km).

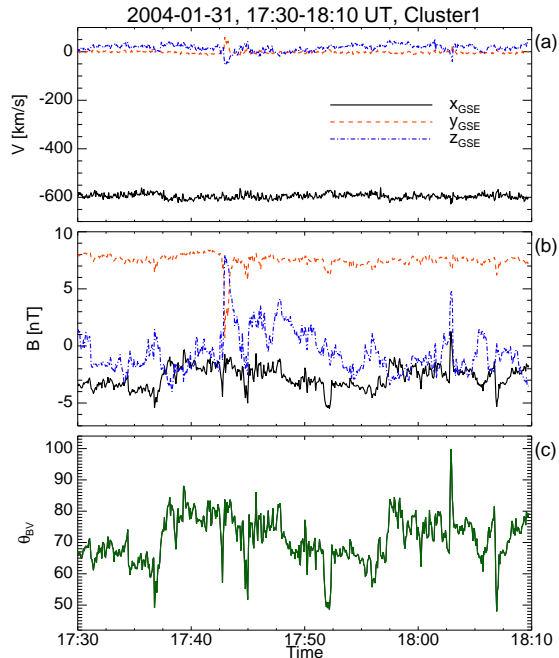


FIG. 1.— Time interval of fast solar wind as measured by the *Cluster1* satellite on January 31st, 2004 (17:30-18:10 UT). Panel (a) and (b) show the velocity, V , and magnetic, B , field components in GSE, respectively; while panel (c) displays θ_{BV} , the angle between the two previous fields.

Figure 1 gives a brief overview of the considered interval from C1. In particular, in panel (a) we show the three components of the velocity field from the Hot Ion Analyser (HIA) sensor of the Cluster Ion Spectrometry (CIS) with a resolution of 4 seconds (Rème et al. 2001). Here, x (black), y (red) and z (blue) denote the Geocentric Solar Ecliptic (GSE) coordinate system, i.e. x component points towards the Sun and z axis is perpendicular to the plane of the Earth’s orbit around the Sun (positive North). The v_y , that is the component in the direction anti-parallel to the direction of Earth’s motion, has been corrected for the ~ 30 km/s aberration produced by the orbital speed of the spacecraft and Earth around the Sun. Moreover, panel (b) displays the raw data of the magnetic field vector, from the Fluxgate Magnetometer (FGM) (Balogh et al. 2001), where the three components are also given in GSE, by using the same colors of panel (a). Although in this case the data are represented with the same resolution of the velocity field in panel (a), i.e with a 4 second resolution, in the following part of the paper we will use the highest sampling time of the FGM instrument in nominal mode (22 Hz) to properly describe ion scales. Finally, panel (c) of Figure 1 shows the temporal evolution of the angle between magnetic and velocity fields, θ_{BV} . The large values of the angle, $\theta_{BV} > 50^\circ$, indicate that the two vectors are approximately perpendicular, suggesting that there is no connection of the analyzed stream of solar wind with the Earth’s foreshock: indeed, the electrostatic waves, typical of a magnetic connection, are not observed on WHISPER during this interval (not shown here).

In order to quantify the turbulence we compute the power spectrum of the magnetic fluctuations, up to elec-

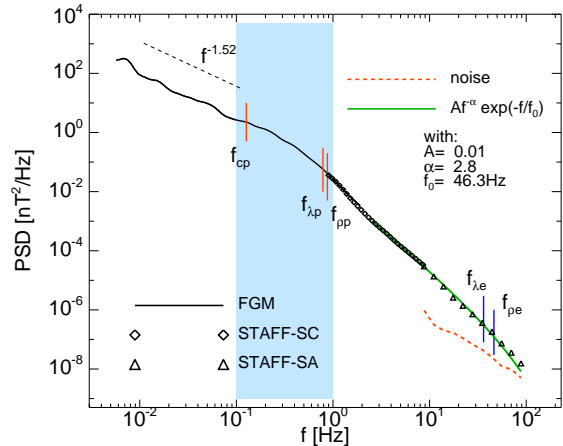


FIG. 2.— Power spectral density of total magnetic fluctuations measured on C1, by FGM (up to ~ 1 Hz, solid line), STAFF-SC (up to ~ 9 Hz, diamonds) and STAFF-SA ($f \geq 8$ Hz, triangles). The red dashed line shows the STAFF-SA noise level on C1. The power-law fit in the MHD range is displayed by the black dashed line, while the spectrum at scales smaller than the ion characteristic scales is described by $Af^{-\alpha} \exp(-f/f_0)$ (green solid line). Vertical solid bars indicate the proton (in red) and the electron (in blue) characteristic scales (assuming $f_{pe} = f_0$), while the blue filled band denotes the range of scales, $f \in [0.1, 1]$ Hz, around ion scales.

tron scales. Figure 2 shows the total power spectral density (PSD), $S(f) = \sum_{i=x,y,z} S_i(f)$, where S_i is the PSD of each component of the magnetic field and is defined as

$$S_i(\tau) = \frac{2\delta t}{N} \sum_{j=0}^{N-1} |\mathcal{W}_i(\tau, t_j)|^2, \quad i = x, y, z \quad (1)$$

begin δt the time spacing and \mathcal{W}_i the Morlet wavelet coefficients for different time scales τ and time t_j (Torrence & Compo 1998)

$$\mathcal{W}_i(\tau, t) = \sum_{j=0}^{N-1} B_i(t_j) \psi^*[(t_j - t)/\tau]. \quad (2)$$

The frequency dependence is easily obtained using the $f = 1/\tau$ relationship.

We use the onboard FGM measurements up to ~ 1 Hz (solid line) and the Spatio Temporal Analysis of Field Fluctuation experiment/Search Coil (STAFF-SC) (Cornilleau-Wehrin et al. 2003), with a resolution of 25 Hz in the frequency domain [0.35–9] Hz (diamonds). Finally, we complete the analysis with the Spatio Temporal Analysis of Field Fluctuation experiment/Spectrum Analyser (STAFF-SA) on C1, which provides 4 seconds averages of the power spectral density of the magnetic fluctuations at 27 logarithmically spaced frequencies, between 8 Hz and 4 kHz (triangles). The red dashed line shows the instrumental STAFF-SA noise level that becomes significant for $f > 88$ Hz, where the signal-to-noise ratio (S/N) is lower than 3. This region is omitted in Figure 2 to avoid any misunderstanding.

The spectrum in Figure 2 shows the characteristic behaviour of the solar wind turbulent cascade (Bruno et al. 2014). At low frequencies, in the MHD range, the distinctive behaviour of a power law, $\propto f^{-1.52}$, is observed

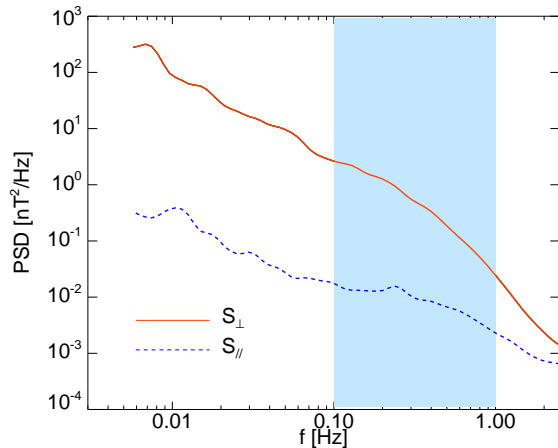


FIG. 3.— Power spectral density of the perpendicular (red solid line) and parallel (blue dashed line) magnetic field fluctuations measured by FGM. The blue filled band denotes the range of scales $f \in [0.1, 1]$ Hz, as in Figure 2.

(black dashed line). Then, around 0.3 Hz, that is in-between the characteristic proton frequencies (i.e., cyclotron frequency, f_{cp} , and Doppler shifted proton Larmor radius, $f_{\rho_p} = v_{sw}/2\pi\rho_p$, and proton inertia length, $f_{\lambda_p} = v_{sw}/2\pi\lambda_p$) estimated under the assumption of wave-vector parallel to the plasma flow (vertical red bars), a change in the spectral shape is observed. At higher frequencies ($f > 0.3$ Hz), the spectrum is steeper and is well described by the exponential model proposed by Alexandrova et al. (2012) for a general description of the whole turbulent spectrum at kinetic scales. The present model

$$PSD(f) = Af^{-\alpha} \exp(-f/f_0) \quad (3)$$

is composed by an exponential with a characteristic frequency f_0 and with a power-law pre-factor. Therefore, the three free parameters are (i) the amplitude A , (ii) the spectral index α and (iii) the cutoff frequency (f_0). The exponential model fitting is shown in Figure 2 by the green solid line, including also the parameters of the fit: $A \simeq 0.01$, $\alpha \simeq 2.8$ and $f_0 \simeq 46.3$ Hz. By considering f_0 related to the Doppler shifted electron Larmor radius, $f_{\rho_e} = v_{sw}/2\pi\rho_e$, in agreement with the general spectrum proposed by Alexandrova et al. (2012), $f_0 \in [0.74f_{\rho_e}, f_{\rho_e}]$, we have $\rho_e \in [1.5, 2.1]$ km. This result is in agreement with ρ_e estimated by using directly the electron perpendicular temperature.

In Figure 2, the blue filled band denotes the range of scales, $f \in [0.1, 1]$ Hz, that are of interest for the investigation of the nature of the turbulent fluctuations around ion scales, which is the aim of the present work. Therefore, in the following part of the paper, we will focus on the high-resolution magnetic field data given by FGM on C1.

Figure 3 shows the PSD of the perpendicular (red solid line) and parallel (blue dashed line) magnetic field fluctuations. The variations of the magnetic field magnitude can be used as a proxy of the parallel (compressive) fluctuations ($\delta B_{\parallel} = \delta|B|^2/2B_0$, where B_0 is the mean magnetic field on the whole interval (Perrone et al. 2016)),

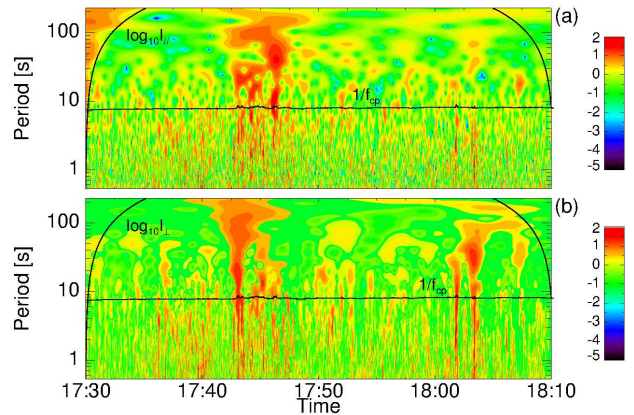


FIG. 4.— Logarithmic contour plots of LIM, $I(\tau, t)$, for parallel (a) and perpendicular (b) magnetic field fluctuations. Horizontal black lines denote the proton cyclotron period, while the curved black lines indicate the cone of influence for the Morlet transform.

so the corresponding energy is

$$\mathcal{W}_{\parallel}^2(\tau, t) = \mathcal{W}_{|B|}^2(\tau, t), \quad (4)$$

while the energy of the perpendicular (Alfvénic) fluctuations is defined as

$$\mathcal{W}_{\perp}^2(\tau, t) = \mathcal{W}_{\mathbf{B}}^2(\tau, t) - \mathcal{W}_{\parallel}^2(\tau, t), \quad (5)$$

where $\mathcal{W}_{\mathbf{B}}^2(\tau, t)$ is the total energy of the magnetic fluctuations. The bias in the spectrum due to the quantization noise, not shown in the Figure, is $q^2/12f_s \sim 4 \cdot 10^{-7}$ nT²/Hz (Widrow & Kollár 2008), being q the digitization of the instrument (10^{-2} nT for FGM in the solar wind mode), f_s the sampling frequency (22 Hz) and by assuming that the noise is uniformly distributed over the entire spectral range. However, although the quantization noise is very low, the comparison between FGM and STAFF data shows that the two spectra start to deviate for $f > 1 - 2$ Hz, meaning that the instrumental noise could become important at frequencies higher than 1 – 2 Hz.

Figure 3 shows that, although in the inertial range the energy stored in the perpendicular direction is much stronger than the compressive one, around ion scales the compressive energy increases, meaning that the contribution of the parallel magnetic fluctuations becomes important at kinetic scales (Alexandrova et al. 2007, 2008; Salem et al. 2012; Kiyani et al. 2013; Perrone et al. 2016) and, in particular, in the frequency range around the spectral transition ($f \in [0.1, 1]$ Hz, blue filled band). The small bump in the compressive energy around 0.25 Hz corresponds to the satellite spin ($\tau = 4$ s).

3. INTERMITTENCY, NON-GAUSSIANITY AND PHASE COHERENCE

The spectra, in general, provide information about the global properties of the turbulent activity, but only a local analysis of the fluctuations enables to understand the details of turbulence. In this context, panels (a) and (b) of Figures 4 show the evolution of the Local Intermittence Measure (LIM) for the parallel and perpendicular magnetic energy, respectively. The LIM is defined as the

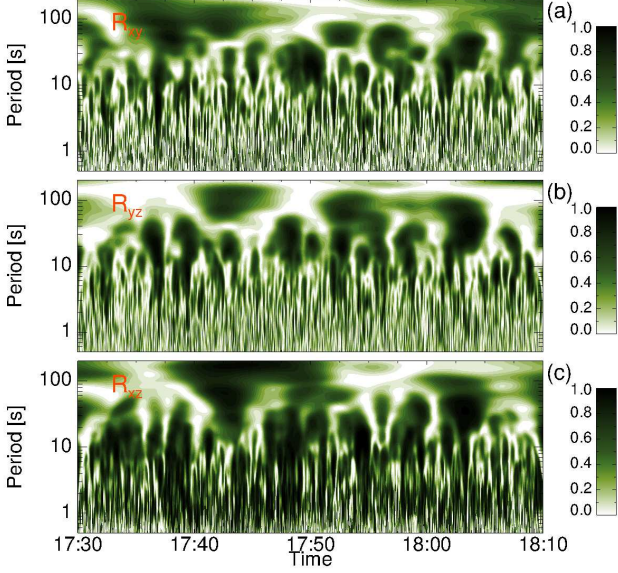


FIG. 5.— Logarithmic contour plots of phase coherence, $R_{ij}(\tau, t)$, for B_x and B_y (a); B_y and B_z (b); and, B_x and B_z (c).

energy of magnetic fluctuations, as a function of time and scales, normalized at each time point by a mean spectrum over the whole time interval:

$$I_{\parallel, \perp}(\tau, t) = \frac{|\mathcal{W}_{\parallel, \perp}(\tau, t)|^2}{\langle |\mathcal{W}_{\parallel, \perp}(\tau, t)|^2 \rangle_t}. \quad (6)$$

The curved black lines, on each side of the plots in Figures 4, represent the cone of influence where the Morlet coefficients are affected by edge effects (Torrence & Compo 1998). Non uniform distribution of energy is observed in both parallel and perpendicular components with the appearance of localized energetic events covering a certain range of scales, which are easily recognized by red color. This is an indication of the presence of coherent structures in the system, that will be described in detail in Section 4. These intermittent events are strictly connected with the strong variations of the magnetic field components (see for example the variation between 17:40 and 17:50 in panel (b) of Figure 1), that is highlighted by the variation of the inverse of the proton cyclotron frequency (horizontal black lines in Figure 4).

Let's consider the phase coupling between the magnetic components during the analyzed time interval. Figure 5 shows the phase coherence, $R_{ij}(\tau, t)$, between two components, B_i and B_j , defined as (Grinsted et al. 2004; Lion et al. 2016)

$$R_{ij}^2(\tau, t) = \frac{|\mathcal{S}(\tau \mathcal{W}_i(\tau, t) \mathcal{W}_j^*(\tau, t))|^2}{\mathcal{S}(\tau |\mathcal{W}_i(\tau, t)|^2) \cdot \mathcal{S}(\tau |\mathcal{W}_j^*(\tau, t)|^2)}, \quad (7)$$

where \mathcal{S} is a compound smoothing operator for frequencies and time, $\mathcal{S}(\mathcal{W}(\tau, t)) = \mathcal{S}_\tau(\mathcal{S}_t(\mathcal{W}(\tau, t)))$, with

$$\mathcal{S}_\tau(\mathcal{W}(\tau, t)) = \mathcal{W}(\tau, t) c_1^{-t^2 \tau^2 / 2} \quad (8)$$

$$\mathcal{S}_t(\mathcal{W}(\tau, t)) = \mathcal{W}(\tau, t) c_2 \Pi(0.6/\tau) \quad (9)$$

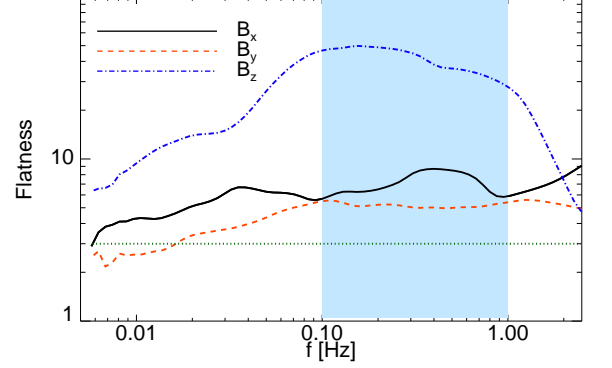


FIG. 6.— Flatness, $\mathcal{F}_i(\tau)$, for B_x (black solid line), B_y (red dashed line) and B_z (blue dot-dashed line). The horizontal green dotted line indicates the value of the flatness for a standard normal distribution, while the blue filled band denotes the range of scales $f \in [0.1, 1]$ Hz.

being c_1 and c_2 the normalization constants (Grinsted et al. 2004), Π the rectangular function and 0.6 the scale decorrelation length for the Morlet wavelet (Torrence & Compo 1998). By definition, the values of $R_{ij}(\tau, t)$ are between 0 (no coherence, in white) and 1 (full coherence, in black).

We consider the phase coherence between magnetic components in a reference frame where z is aligned with a magnetic field \mathbf{B}_0 averaged on the whole time interval ($\mathbf{e}_z = \mathbf{e}_b$); x is perpendicular to \mathbf{B}_0 in the plane spanned by it and the radial direction ($\mathbf{e}_x = \mathbf{e}_b \times \mathbf{e}_r$); and y closes the right-hand reference frame ($\mathbf{e}_y = \mathbf{e}_b \times \mathbf{e}_x$). In this case, we are considering the global frame defined on 40 minutes. In Sections 4 and 5 a local frame will be assumed by considering a magnetic field at scales on the same order of scales of the individual turbulent structures. It is worth pointing out that the choice of a particular mean magnetic field could lead to significant differences in physical results (Chen et al. 2011; Matthaeus et al. 2012; TenBarge et al. 2012). However, in our case, both the magnetic frames produce almost the same results since the angle between the global and the local magnetic field is small (its histogram, not shown here, is peaked around 10°).

Figure 5 shows the phase coherence of each couple of magnetic field components, where localized regions in time of high coherence are found, that cover a certain range of scales, including the frequency range $f \in [0.1, 1]$ Hz ($\tau \in [1, 10]$ s), as in the case of intermittency for both perpendicular and parallel magnetic energy (Figures 4).

Keeping the same reference frame, we investigate the Gaussianity of the magnetic fluctuations as a function of scale (or frequency) by using the fourth-order moment of each component. We define the flatness (or kurtosis) of B_i as

$$\mathcal{F}_i(\tau) = \frac{\langle \tilde{\mathcal{W}}_i(\tau, t)^4 \rangle}{\langle \tilde{\mathcal{W}}_i(\tau, t)^2 \rangle^2}, \quad (10)$$

where $\tilde{\mathcal{W}}$ is the real part of the wavelet coefficient and $\tau = 1/f$. If $\mathcal{F}_i(\tau) = 3$, the probability distribution function (PDF) of the corresponding component of magnetic field fluctuations is a standard normal distribution, while

if $\mathcal{F}_i(\tau) > 3$ the PDF is not a Gaussian distribution, showing fat tails.

Figure 6 shows $\mathcal{F}_i(f)$ for B_x (black solid line), B_y (red dashed line) and B_z (blue dot-dashed line). The value of the flatness for a standard normal distribution (horizontal green dotted line) is given as reference. We observe that the flatness of both parallel and perpendicular magnetic field fluctuations departs from the normal distribution value, reflecting a non-homogeneous distribution of the turbulent fluctuations as already observed in the maps of the LIM (Figure 4). Moreover, after an initial increase of \mathcal{F}_i , the flatness of both perpendicular (\mathcal{F}_x and \mathcal{F}_y) and parallel (\mathcal{F}_z) fluctuations becomes nearly constant around ion scales (blue filled band). However, for $f \sim 1$ Hz, i.e. where the FGM data start to deviate from STAFF data, \mathcal{F}_z becomes to decrease. This behaviour could be due to the fact that the noise becomes to be important for $f > 1 - 2$ Hz. Indeed, the noise is expected to have Gaussian statistics; thus, \mathcal{F}_z might approach the constant value expected for a Gaussian distribution. However, a decrease in flatness, related to the frequency location of the break, has been already observed in literature by Wu et al. (2013) and Telloni et al. (2015). In particular, Wu et al. (2013) observed a flatness decrease in all the magnetic components, arguing that it is of physical origin, due to an additional ingredient of incoherent dynamics.

Therefore, in addition to the intermittency and phase coherence, the ion scales appear also characterized by the departure from Gaussianity of the PDFs. However, the expected behavior for the intermittency to increase decreasing the scales is not observed in these particular range of scales, where the flatness is almost constant. Moreover, it is worth pointing out that \mathcal{F}_z reaches a higher value of saturation with respect to \mathcal{F}_x and \mathcal{F}_y (even though most of the energy is stored in the B_x component), meaning that the parallel direction could represent a preferential channel for the evolution of nonlinear effects at kinetic scales.

To focus on the range of scale around ion scales and to compare the present analysis with the results in slow solar wind described in Perrone et al. (2016), we use a bandpass filter based on the wavelet transform (Torrence & Compo 1998; He et al. 2012; Roberts et al. 2013; Perrone et al. 2016) for the range $f \in [0.1, 2]$ Hz, defined as

$$\delta b_i(t) = \frac{\delta j \delta t^{1/2}}{C_\delta \psi_0(0)} \sum_{j=j_1}^{j_2} \frac{\tilde{W}_i(\tau_j, t)}{\tau_j^{1/2}}, \quad (11)$$

where j is the scale index and δj is the constant step in scales; the factor $\psi_0(0) = \pi^{1/4}$ and the value of the constant C_δ , derived from the reconstruction of a δ function using the Morlet wavelet, is 0.776 (Torrence & Compo 1998). Finally, $\tau(j_1) = 0.5$ s and $\tau(j_2) = 10$ s.

Figure 7 displays the PDFs of δb_x (a), δb_y (b) and δb_z (c), normalized to their own standard deviations, $\sigma(\delta b_i)$, whose values are indicated in the corresponding panels. Most of the energy is stored in the perpendicular directions, as already observed in the spectra for both perpendicular and parallel magnetic fluctuations (Figure 3). The PDFs are compared to their corresponding Gaussian fits (black dashed lines), showing the presence

of fat non-Gaussian tails in each component of magnetic field fluctuations with respect to the background magnetic field, especially in the z direction as expected from the higher values of \mathcal{F}_z with respect to \mathcal{F}_x and \mathcal{F}_y . The vertical black solid lines in each panel indicate the position of three standard deviations of the Gaussian fit for the corresponding magnetic fluctuations, which include 99.7% of the Gaussian contribution. All the events that exceed these limits, $|\delta b_i| > 3\sigma_G(\delta b_i)$, contribute to the non-Gaussian part of the PDFs.

To investigate the relation between the non-Gaussianity of the magnetic fluctuations and the phase coherence between the components, in Figure 8 we consider about 40 seconds out of 40 minutes of the whole interval of fast solar wind. Panel (a) shows the time evolution of turbulent magnetic fluctuations δb_x (black line), δb_y (red line) and δb_z (blue line), as defined in eq. (11). In panel (b) we display the total turbulent magnetic energy, $\delta b_{tot}^2 = \delta b_x^2 + \delta b_y^2 + \delta b_z^2$, where the red horizontal dashed line indicates the threshold, which will be considered in the following part of the paper to select intermittent events. The threshold is defined as 3σ of the distribution law for the amplitudes of a Gaussian vectorial field compared to δb_{tot}^2 . Finally, in panel (c) we show $R_{ij}(f_0, t) > 0.6$ for the highest frequency considered in the selection of intermittent events ($f_0 = 2$ Hz). One can see that we observe very strong peaks of coherence, i.e. magnetic field components are strongly coupled. These peaks are localized in time and very often (e.g. between 20 and 30 s) they correspond to strong peaks in magnetic energy (see panel (b)). However, sometimes strong coherence between two components, e.g. ~ 10 s, corresponds to small amplitude in δb_{tot}^2 , that is not selected by our threshold, that could be overestimated to select all the coherent structures.

This result verifies the link between intermittency, non-Gaussian fluctuations and phase coherence between magnetic field components, in agreement with the studies of Koga et al. (2007) and Lion et al. (2016). Moreover, thanks to this link, we can assert that the selection of intermittent events in a turbulent signal is almost independent of the choice of a particular magnetic field component, as far as all components are coupled.

In the present paper, we select intermittent events by considering a threshold (~ 1.2 nT²) on the total turbulent magnetic energy, δb_{tot}^2 , in the range scale $f \in [0.1, 2]$ Hz, as discussed above. It is worth pointing out that the same results, that will be described in the following part of the paper, can be found if we select intermittent events by considering compressive fluctuations, $\delta b_{||} = \delta|b|$, as in Perrone et al. (2016). For the whole time interval (40 minutes) of fast solar wind, we get about 140 peaks, meaning that coherent structures cover $\sim 30\%$ of the analyzed stream (where the coherent time is evaluated as 2.5 times the time scale of each structure, without overlapping¹). In fast solar wind the coherent structures appear to be somewhat less frequent with respect to the interval of slow solar wind described in Perrone et al.

¹ Looking at each structure recovered by the selection method, we observe that coherent fluctuations are somehow larger than the time scale, defined as the time range between two minima containing a maximum of energy over the threshold. The same definition of coherent time has been used in Perrone et al. (2016).

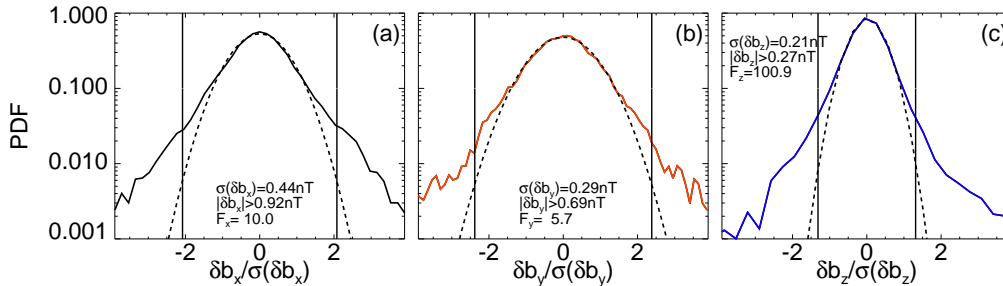


FIG. 7.— PDFs of δb_x (a), δb_y (b) and δb_z (c), normalized to their own standard deviations, $\sigma(\delta b_i)$, and compared to their corresponding Gaussian fits (black dashed lines). Vertical black solid lines show the position of three standard deviations of each Gaussian fit. The values of $\sigma(\delta b_i)$, the limits for the Gaussian contribution, $3\sigma_G(\delta b_i)$, and the flatness, \mathcal{F}_i , are also indicated in each panel.

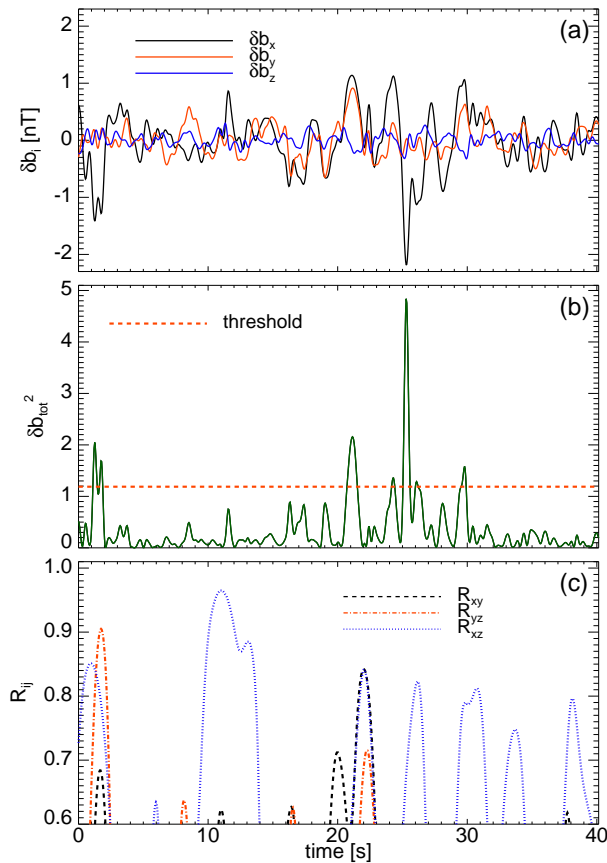


FIG. 8.— Panel (a): Temporal evolution of turbulent magnetic fluctuations, δb_i (see eq. 11), in a considered zoom of about 40 s. Panel (b): Total magnetic energy, δb_{tot}^2 , where the red horizontal dashed line indicates the threshold of intermittent events. Panel (c): Phase coherence $R_{ij}(f_0, t) > 0.6$ with $f_0 = 2$ Hz, being the highest frequency considered for the magnetic fluctuations.

(2016), in which $\sim 40\%$ of the interval was covered by coherent events. A detailed analysis of the structures in fast solar wind will be presented in the following Sections of the paper.

4. COHERENT STRUCTURES

To study the nature of the intermittent events, we perform a minimum variance analysis around each selected peak, identifying magnetic fluctuations which are well-localized in space and with regular profiles. These characteristics are inherent properties of coherent structures. However, since the automatic method for the selection of intermittent events recovers the most energetic peaks, it is possible that if there are few of them very close they refer to the same event. In order to avoid an overestimation of the detected events, we check all the selected peaks and we confidently identify 101 events. In particular, we find 19 isolated vortices, 32 vortex chains and 18 current sheets. For the latter, only 6 current sheets are isolated, while the other 12 are recovered at the center of vortices or sometimes at their boundaries. Moreover, for the remaining 32 structures the nature is not clear. However, no strongly compressive structures, such as solitons, magnetic holes or shocks, have been detected, in stark contrast to what is observed in slow solar wind.

In the following, we present three examples of observed coherent structures of different nature. In Figures 9, 11 and 13, panels (a) display the modulus of the raw magnetic field measurements, namely large scale magnetic field, as observed by the four satellites (different line styles), where the FGM noise at $f > 2.5$ Hz is taken off. The red double arrow indicates $\Delta\tau$, i.e. the characteristic temporal scale of the structures (see Perrone et al. (2016) for the details), while the two vertical dashed lines denote the total width of the structures ($\Delta\tau'$).

Panels (b) show magnetic fluctuations δb_i (with $i = x, y, z$), defined by eq. (11), in a BV -reference frame which takes into account the directions of the local mean magnetic field \mathbf{b}_0 and flow velocity \mathbf{v}_0 evaluated within each structure time scale $\Delta\tau'$: z is aligned with \mathbf{b}_0 , $\mathbf{e}_z = \mathbf{e}_b$ (blue lines), x is aligned with \mathbf{v}_0 in the plane perpendicular to \mathbf{b}_0 , $\mathbf{e}_x = (\mathbf{e}_b \times \mathbf{e}_v) \times \mathbf{e}_b$ (black lines), and y closes the right-hand reference frame, $\mathbf{e}_y = \mathbf{e}_b \times \mathbf{e}_x$ (red lines). The time of each satellite is shifted taking into account the time delays with respect to C1. Moreover, panels (c) display the evolution of the current density \mathbf{J} , calculated by using the curlometer technique (Dunlop et al. 1988, 2002), based on four-point measurements of *Cluster*. The three components of \mathbf{J} are given in the BV -frame, while the modulus, $|\mathbf{J}|$, is shown by dashed line.

To have information on the plasma quantities, panels (d) show the behaviour of the electron density, n_e , evaluated by using the satellite potential (Pedersen 1995; Pedersen et al. 2001) from the Electric Field and Wave

(EFW) experiment (Gustafsson et al. 1997). These measurements have 5 vectors per second time resolution, that is much better than particle measurements on Cluster, which have 4 seconds time resolution. However, the spacecraft potential is subject to a strong spin effect as well as charging effects due to different parts of the spacecraft being illuminated as it spins. In order to have sub-spin time resolution the spin effect needs to be removed. This can be done provided the density is stable by constructing a series of phase angles for the spacecraft, and binning the corresponding potentials by angle as opposed to time. By using the median value of each bin to reduce the effects of extreme values and subtracting the mean in the interval studied the charging fluctuation can be obtained as a function of phase angle. This can be fitted with a model and subtracted from the potential measurement at each spacecraft phase angle. More details are provided in Roberts et al. (2017).

Finally, panels (e) and (f) give the configuration of the four *Cluster* satellites in the BV -frame, by using different symbols and colors: black diamonds for C1, red triangles for C2, blue squares for C3 and green circles for C4. The arrows display the directions of the normal of the structures, \mathbf{n} (black), determined by using the timing method (see Section 5), of \mathbf{v}_0 (red) and of \mathbf{b}_0 (blue). Moreover, the black-dashed lines indicate the plane of the structures.

4.1. Current sheet

The first example of coherent structure is shown in Figures 9. It is an incompressible structure with a component, δb_y , which changes sign and is perpendicular to the local magnetic field. The other two components have fluctuations of very small amplitude. The reversal of the component of maximum variation is in the middle of the structure, where the large scale magnetic field has its local minimum (panel (a)) and a peak in the current is recovered (panel (c)). Minimum variance analysis applied to this structure confirms the result that is a one-dimensional (i.e. linearly polarized) alfvénic structure: the direction of the maximal variation \mathbf{e}_{\max} is perpendicular to the direction of \mathbf{b}_0 ($\theta_{\max} \simeq 86^\circ$), while the current density is almost parallel. The four satellites observe the same amplitudes for the fluctuations, that is consistent with a planar geometry. Moreover, in the center of the structure, a peak in the density is found (panel (d)), meaning that the plasma is confined inside the structure. This event can be identified as a current sheet. Finally, panels (e) and (f) show that the normal to the structure, \mathbf{n} , is almost perpendicular to \mathbf{b}_0 , while is almost parallel to \mathbf{v}_0 . The thickness of the current sheet, estimated by using the timing method (see Perrone et al. (2016) for details), is $\Delta r \simeq 2.5\rho_p$ ($\Delta r' \simeq 13.5\rho_p$, being the total extension of the structure), and its velocity in the plasma frame is $\mathcal{V}_0 \simeq -(23 \pm 209)$ km/s. Therefore, it is almost convected by the flow, as expected for a current sheet.

A well-known one-dimensional current sheet equilibrium is the Harris current sheet (Harris 1961), which is a stationary solution of the Maxwell-Vlasov system. This simple model could represent analytically thin current layers at kinetic scales (Greco et al. 2016). The magnetic field profile is given by a 1D hyperbolic-tangent profile ($B = B_0 \tanh(x/L)$), where x is the spatial co-

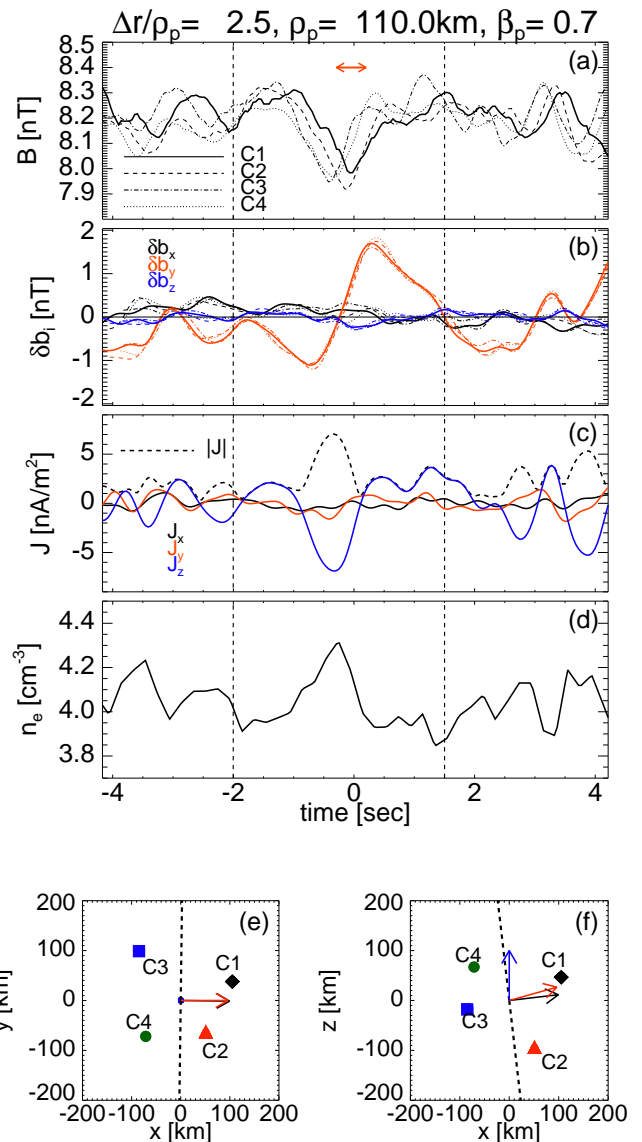


FIG. 9.— Example of a current sheet, centered at 18:03:36 UT. Panel (a): modulus of the large scale magnetic field observed by the four *Cluster* satellites (different style lines). The red double arrow indicates Δr , corresponding to $\Delta r'$, being the characteristic scale of the structure. Panel (b): components of magnetic fluctuations defined by eq. (11), in BV -frame. The time of each satellite is shifted taking into account the time delays with respect to C1. The horizontal black solid line is given as a reference for $\delta b_i = 0$ nT. Panel (c): modulus (black-dashed line) and components (in BV -frame) of the current density. Panel (d): electron density obtained by the spacecraft potential. The vertical black-dashed lines indicate $\Delta r'$, corresponding to the total extension of the structure ($\Delta r' \simeq 13.5\rho_p$). Panels (e) and (f): Configuration of *Cluster* satellites in BV -frame: black diamonds for C1, red triangles for C2, blue squares for C3 and green circles for C4. The arrows indicate the direction of the normal (black), local flow (red) and local magnetic field (blue), while the black-dashed lines represent the plane of the structure.

ordinate and L is the half-width of the current sheet. The corresponding profile for the current density is $J \propto (B_0/L) \cosh^{-2}(x/L)$. Figure 10 shows the three components of the magnetic field fluctuations (panel (a)) and of the current density (panel (b)) in the BV -frame for the discontinuity in Figure 9, as a function of the spatial

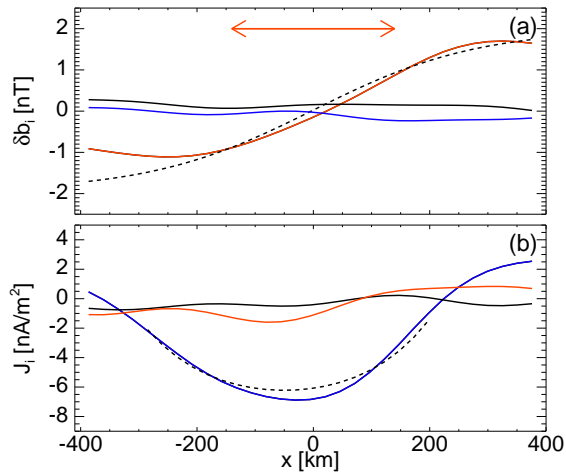


FIG. 10.— Three components of magnetic field fluctuations (panel (a)) and current density (panel (b)) in the BV -frame of the discontinuity in Figure 9, as a function of the spatial coordinate, defined as $x = V * t$. The dashed lines denote the Harris profile for both magnetic field and current, while the red double arrow indicates Δr in km.

coordinate, defined as $x = V * t$, where V is the velocity of the current sheet in the satellite frame and t is the time as indicated in Figure 9. The dashed lines denote the Harris profile for both magnetic field and current, while the red double arrow indicates the characteristic scale of the structure in km, Δr . The agreement between the plasma equilibrium theory and the observed current sheet is satisfactory. The parameters of the fit for δb_y give $B_0 \sim 2nT$, which corresponds approximately to the level of saturation before and after the reversal of the magnetic field. Moreover, from the fit we obtain $L \sim 272 \text{ km} = 2.47\rho_p$, while the characteristic scale of the current sheet from the timing analysis is $\Delta r \simeq 279 \text{ km} = 2.54\rho_p$.

It is worth pointing out that the assumptions behind the analytical model of the Harris current sheet establish that the velocity distributions for both ions and electrons must be Maxwellian. However, the considered stream of fast solar wind is characterised by anisotropic proton temperatures. Unfortunately, due to the low-resolution of ion measurements on *Cluster* (4 seconds), it is not possible to test anisotropic kinetic models.

4.2. Vortex

Another example of coherent structure observed in this stream of fast solar wind is shown in Figure 11. The background magnetic field (panel (a)) is characterized by a modulated fluctuation, observed by the four spacecraft, with a local maximum in the middle of the structure. The corresponding fluctuations, δb_i , are more localized, with the principal variation in the plane perpendicular to the local magnetic field, δb_y , and small compressive fluctuations, $\delta b_z \ll \delta b_y$. Moreover, a minimum variance analysis indicates that the intermediate component is not negligible, i.e. the event is a bi-dimensional structure, and both the directions of maximum and intermediate variance are in the plane perpendicular to \mathbf{b}_0 ($\theta_{max} \simeq 88^\circ$ and $\theta_{int} \simeq 87^\circ$), while the direction of minimum variance is along \mathbf{b}_0 ($\theta_{min} \simeq 3^\circ$). Panel (c) displays

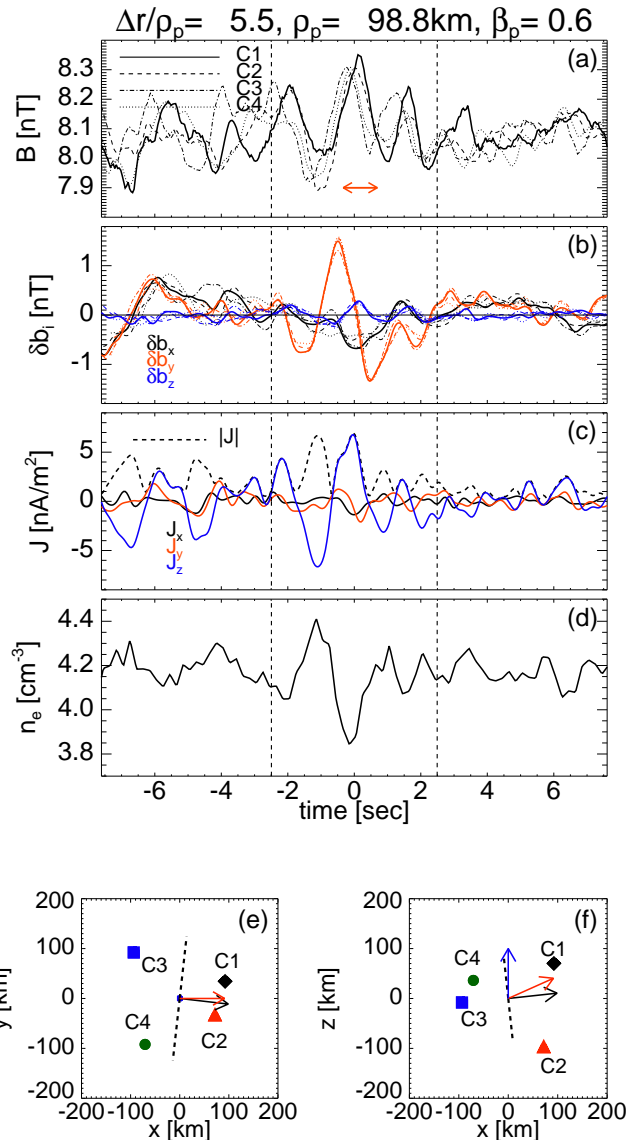


FIG. 11.— Example of a vortex-like structure, centered at 18:06:03.6 UT and with $\Delta r' \simeq 27\rho_p$. The panels are the same as in Figure 9.

the current density, \mathbf{J} , that is mainly in the direction parallel to \mathbf{b}_0 , while panel (d) shows the electrons density, that exhibits a fluctuating behaviour ($\delta n_e \sim 0.1 \text{ cm}^{-3}$) and it is anti-correlated with the background magnetic field, with a local minimum in the center of the structure. Finally, panels (e) and (f) show the result of the timing method for the normal of this structure, that is almost perpendicular to \mathbf{b}_0 ($\theta_{nB} \simeq 84^\circ$), while is almost parallel to \mathbf{v}_0 . The velocity of propagation along the normal and in the plasma frame is $\mathcal{V}_0 \simeq -(27 \pm 240) \text{ km/s}$. The characteristic scale for this two-dimensional structure is $\sim 5.5\rho_p$, while the total width, corresponding to $\Delta\tau'$, is $\sim 27\rho_p$.

The structure looks like a monopolar Alfvén vortex (Petviashvili & Pokhotelov 1992; Alexandrova 2008), crossed by the four satellites more or less at the same distance from the center. In general, a monopolar vortex is a tubular structure which is aligned with the mag-

netic field direction and is a nonlinear analytical solution of the ideal, incompressible MHD equations. However, in this case, the structure shows a pressure balance, i.e. an anti-correlation between density and magnetic field, not predicted by the incompressible model. To verify the vortex topology of this structure, we fit the observed fluctuations with the analytical model for a monopolar Alfvén vortex, derived from the vector potential, \mathbf{A} (Petviashvili & Pokhotelov 1992; Alexandrova 2008; Roberts et al. 2016). The longitudinal current is given by $\mathbf{J} = \nabla_{\perp}^2 \mathbf{A}$.

The vortex is modeled in the $x' - \eta$ plane which are two directions perpendicular to the vortex axis and the x' axis makes an angle of 10° with the relative path of the spacecraft through the plasma. Moreover, the angle of the vortex axis with respect to the magnetic field direction is 2° . The vortex is modeled with a constant amplitude of $A_0 = -0.3$ and the vortex diameter is set at $30\rho_p$. This is motivated by the value obtained from timing analysis and is much larger than the inter-spacecraft distances, consistent with all spacecraft seeing similar fluctuations. Finally, the impact parameter, i.e. the distance from the center at $x' = 0$ is $-0.05a$, being a the radius of the vortex.

Panels (a) and (b) of Figure 12 show the perpendicular fluctuations of the vortex solution $\delta b_x(x', \eta)$ and $\delta b_y(x', \eta)$, respectively, normalized to the local mean magnetic field, \mathbf{b}_0 , while panel (c) shows the normalized longitudinal current, $\delta J_z(x', \eta)$. The spatial dimensions are given in units of the proton Larmor radius, ρ_p . The relative path of the virtual spacecraft is denoted by the arrows. The analytical solution of the Alfvén vortex and *Cluster* data are compared in panels (d)–(f) of Figure 12 and show a good agreement for both magnetic components and current density.

We observe 19 structures similar to the example in Figure 11. Moreover, only 2 of them present a compressive nature, where the ratio between the parallel and perpendicular magnetic field fluctuations is higher than 0.35 (Perrone et al. 2016).

In order to figure out on the possible nature of these structures, we perform an analysis on the polarization (He et al. 2011, 2012; Telloni et al. 2015), though here we are studying structures and not waves (we have not a specific frequency for them, but a range of scales is covered). For all the vortices (except for one) we find, in the satellite frame and in the $(\delta b_y - \delta b_z)$ plane perpendicular to the normal, an elliptical polarization with the major axis perpendicular to the local mean magnetic field, right-handedness with respect to the direction of the normal (that in the wave approximation represents the \mathbf{k} direction). This result is consistent with previous studies of the dissipation range (Goldstein et al. 1994, e.g.) and with the fact that in the case of an Alfvén wave, the increase of the angle between \mathbf{k} and \mathbf{B}_0 produces a change in the polarization from left- to right-handed polarization (Gary 1986).

However, by considering the polarization in the plasma frame (i.e. by considering the sign of \mathcal{V}_0), the result changes. If the velocity of the structure is smaller than the velocity of the solar wind along the normal, the propagation is antiparallel to the normal, so the observed polarization is inversed in the plasma frame (i.e. left-

handed polarization). Since the observed vortices have both positive and negative \mathcal{V}_0 , the polarization can be both right- and left-handedness in the plasma frame. Anyhow, sometimes the value of \mathcal{V}_0 can be very small and/or its error be important. Therefore, a definitive conclusion is very difficult.

Finally, we compare the ratio between the parallel and the total magnetic energy with what expected for Kinetic Alfvén Waves (Boldyrev et al. 2013). In the case of the vortices the ratio is very low, i.e. about one order of magnitude lower than expected for Kinetic Alfvén Waves.

4.3. Vortex chain?

The last example of observed structure is given in Figure 13. The large scale magnetic field is characterized by different oscillations and the same behaviour is observed in the components of the magnetic field fluctuations in panel (b), showing significative oscillations in the plane perpendicular to \mathbf{b}_0 ($\theta_{max} \simeq 88^\circ$ and $\theta_{int} \simeq 84^\circ$), while the minimum variance direction is almost parallel to \mathbf{b}_0 ($\theta_{min} \simeq 7^\circ$) as the current density. Moreover, the principal spatial gradient is $\nabla_{\perp} \gg \nabla_{\parallel}$, which gives $\mathbf{n} \perp \mathbf{b}_0$ (see panels (e) and (f)). Furthermore, the normal of the structure is almost parallel to \mathbf{v}_0 and the velocity of propagation in the plasma rest frame is $\mathcal{V}_0 \simeq -(52 \pm 580)$ km/s. The characteristic scale for this structure, indicated by the red double arrow, is $\sim 6.1\rho_p$, while the total width is $\sim 89\rho_p$. Finally, as in the case of the vortex in Figure 11, the electron density (panel (d)) is anti-correlated to the large scale magnetic field, meaning that also this event is in pressure balance.

Figure 14 shows five incomplete electron pitch angle distributions, taken during about 20 seconds surrounding the center of the structure. In particular, these plots are cuts of the distribution at pitch angles 0° (blue line), 90° (black line) and 180° (red line). Some gaps in the lines are due to missing data. Moreover, the electron pitch angle distributions are not corrected from the spacecraft potential also because of missing data. However, the spacecraft potential is less than 9 eV since this is the lowest energy PEACE measures and no photoelectrons are visible.

In its most common operating mode, the PEACE electron spectrometer (Johnstone et al. 1997; Fazakerley et al. 2009) returns a 2D pitch angle distribution from one or both of its two sensors every spacecraft spin (i.e. ~ 4 s). Each pitch angle distribution is constructed from two energy sweeps taken two seconds apart, when a sensor's field of view is looking along and against the magnetic field direction, respectively. An individual sweep is typically completed in ~ 0.125 s. Thus, it is possible to examine the electron properties of small-scale structures using PEACE, albeit without complete pitch angle coverage, by considering an individual sweep that was taken during the passage of that structure over the spacecraft.

In Figure 14 the time of the cuts corresponds to the vertical green dot-dashed lines in Figure 13 for pitch angles 90° and 180° , while pitch angle 0° is taken 2 s later. We observed a typical strahl signature for pitch angle 0° in each panel of Figure 14, meaning that it does not change over all the considered 20 minutes. No information is available in panel ii due to the loss of coverage.

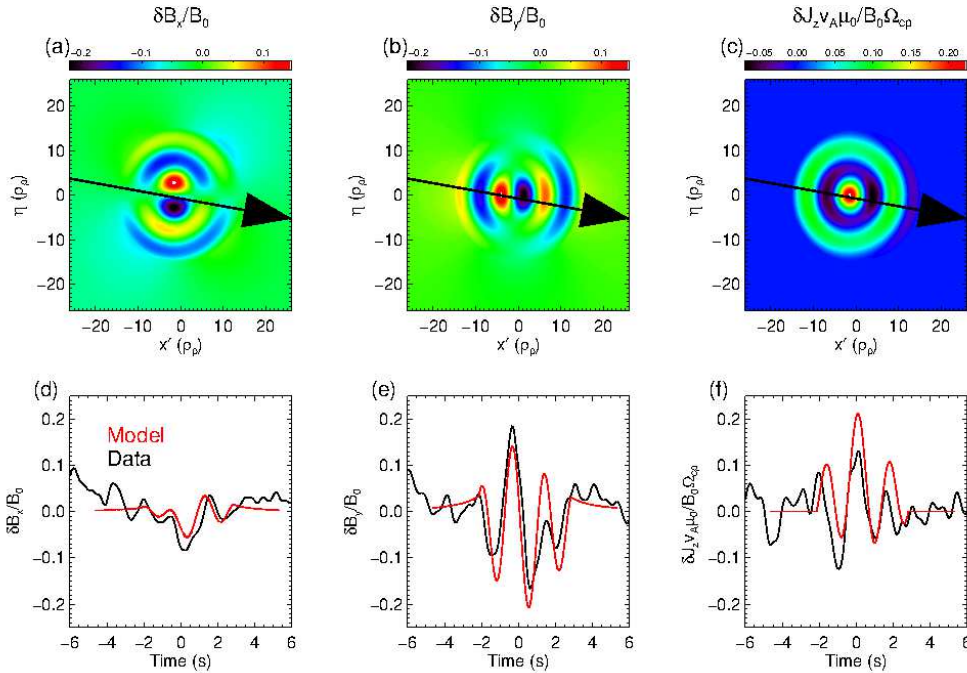


FIG. 12.— Quasi-monopolar Alfvén vortex model for the fluctuations in Figure 11. Panels (a) and (b) show the perpendicular fluctuations of the vortex solution $\delta b_x(x', \eta)$ and $\delta b_y(x', \eta)$, respectively, normalized to the local mean magnetic field, \mathbf{b}_0 , while panel (c) shows the normalized longitudinal current, $\delta J_z(x', \eta)$. The spatial dimensions are given in units of proton Larmor radius, ρ_p . The arrows denote the paths of the spacecraft through the vortex which give the modeled fluctuations (red lines) in panels (d)–(f).

Let's consider now the electron distributions for pitch angles 90° and 180° . Panels iii and iv of Figure 14 are from two sweeps taken at the center of the structure ($t = 0$) and 4 seconds later ($t = +4$ s), respectively. At these times, that correspond to the vortex central region, the electron distributions seem to be typical solar wind distribution: almost isotropic with a spectral break between the core and the halo at about 60 eV. No evidence of accelerated particles or beams is observed. Moreover, in panel iv there is no data from pitch angle 90° because at that time the magnetic field direction changes significantly, losing coverage.

A different situation is found close to the vortex boundary ($t = -4$ s and $t = +8$ s), where the theoretical current model for a vortex presents a discontinuity. Here, in panels ii and v, the electron distributions are atypical, with an increase in the phase space density, localized in energy at ~ 100 eV, in both antiparallel and perpendicular electrons. These distributions could be unstable and generate waves, such as Langmuir waves. Finally, panel i shows the electron distribution at $t = -8$ s, that is close to a current sheet or another vortex boundary and is slightly atypical, with an increase in the phase space density around ~ 100 eV for pitch angle 180° .

The structure in Figure 13 could be interpreted as a chain of three adjacent vortices, crossed by the spacecraft at different distance from the center of each vortex. It is interesting that, within the vortices, the electron distribution functions are typical solar-wind distributions but, close to their boundaries, electrons beams are observed at pitch angles 90° and 180° , while in pitch angle 0° we do not see any changes. However any signature of a similar amplitude to those observed in pitch angles 90° and 180° would be small compared to the signature

of the strahl. Unfortunately, due to the low time resolution of the measurements, we are not able to follow the evolution of the electron pitch angle distribution in each point of the structure. Even worse is the case of ion measurements, whose time resolution on the considered solar wind stream is so low (~ 1 minute in the low geometric factor side of the HIA instrument for solar wind measurements) that no detailed information are available and also the angular resolution is still quite low to study the deformation of the velocity distribution (B. Lavraud 2017, private communication).

On the other hand, the structure could be also described as an interaction between vortices. By assuming, for example, that the two initial vortices are centered around -5 and 5 s with an isolated extension of about 8 s each, we could expect that the center of the total structure corresponds to the region of interaction. From panel (c), the signs of the vortex currents suggest that the Lorentz force could attract the two vortices. Moreover, looking at the shape of the magnetic fluctuations in panel (b), it seems that the vortex on the left side is more distorted with respect to the right one. This could be due to different and opposite velocities of the vortices (higher for the vortex on the right side) or to the different initial amplitudes of the vortices, that produce a different level of distortion at this stage of the interaction. This stage, in fact, could be only a transition phase for this interaction between vortices and this configuration could collapse later in a single larger vortex (Novikov & Sedov 1979).

5. MULTI-SATELLITE ANALYSIS

The Cluster mission provides a unique opportunity to determine the three-dimensional, time-dependent characteristics of small-scale structures, using four-point

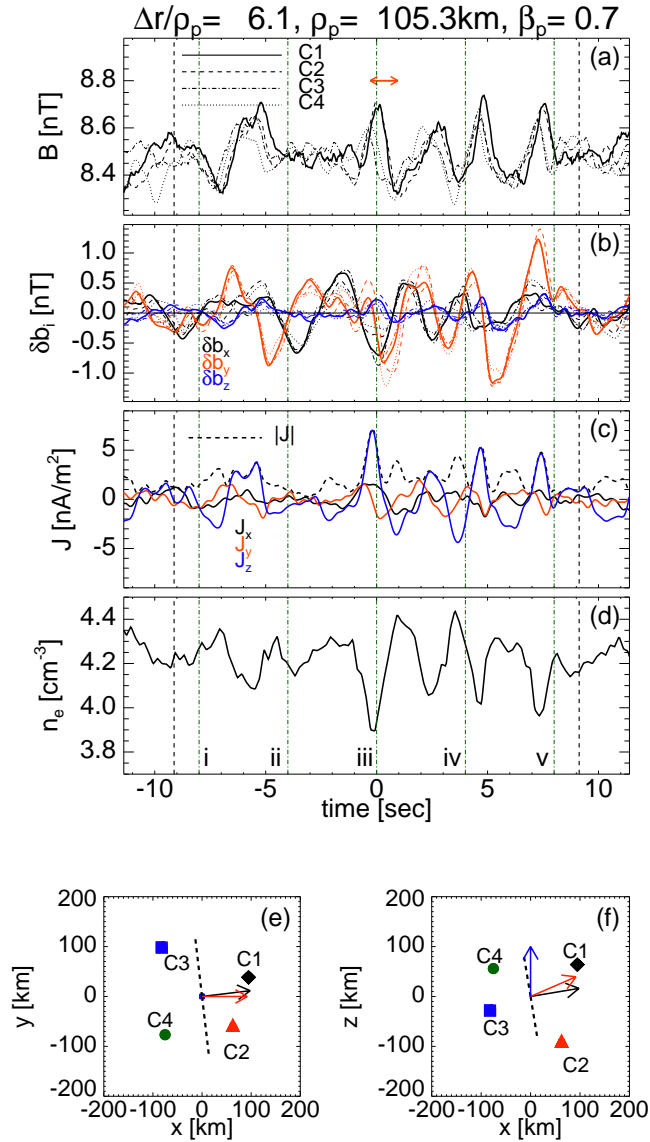


FIG. 13.— Example of an interaction of Alfvén vortices, centered at 17:37:33.6 UT and with $\Delta r' \simeq 89\rho_p$. The panels are the same as in Figure 9. Moreover, the vertical green dot-dashed lines in each panel denote the time of the electron pitch angle distributions in Figure 14.

measurements given by identical instrumentation on the four satellites. Indeed, multi-spacecraft observations exhibit a connection between space and time: the same physical observables are measured not only at different points in space, but also at different instants in time. To exploit this opportunity, we use the *timing* method (Schwartz 1998; Perrone et al. 2016) to characterize the coherent structures observed in this interval of fast solar wind.

The timing method is based on time and space separations and allows to determine the velocity, \mathcal{V} , and the direction of propagation, \mathbf{n} , of a locally planar structure moving with a constant speed in the spacecraft frame. All the details about the method and the conditions of its validity can be found in Section 4.2 of Perrone et al. (2016). In the present work, the timing technique allows us to study only a subset of 33 structures (out of 101),

for which the method keeps validity and we are sure to properly determine \mathbf{n} and \mathcal{V} .

Figure 15 shows the distributions of the angles between the local magnetic field \mathbf{b}_0 and several vectors, i.e. the normal of the structure, the directions of maximal and minimum variance, and the distribution of the angle between \mathbf{n} and the local solar wind velocity in the perpendicular plane, to statistically characterize the geometry and the properties of the observed coherent structures. In particular, θ_{nB} (black solid line) is always close to $\sim 90^\circ$, meaning that all the observed coherent structures have a perpendicular wave-vector anisotropy ($k_\perp \gg k_\parallel$), while θ_{nV_\perp} (green solid line) is peaked around $\sim 20^\circ$, where V_\perp is the local solar wind velocity in the (x, y) -plane of the BV -reference frame. These results are in agreement with the case of slow solar wind studied by Perrone et al. (2016). On the other hand, \mathbf{e}_{\min} (red dashed line), the angle between \mathbf{b}_0 and the direction of minimal variance, shows a uniform distribution in the range between 0° and 80° . Moreover, θ_{max} (black solid line), the angle between \mathbf{b}_0 and the direction of maximal variance, is almost peaked around $\sim 90^\circ$, emphasizing the absence of compressive structures in fast solar wind. Here, the structures are mostly Alfvénic ($\delta b_\perp \gg \delta b_\parallel$) with very small compressive component with respect to slow solar wind structures. These results, in comparison with the analysis done by Perrone et al. (2016), suggest a different nature, in terms of features of coherent structures, between fast and slow streams of solar wind.

To study more in detail the differences between the two streams, in Figure 16, we statistically investigate the velocity of the structures along the normal direction in the plasma frame, $\mathcal{V}_0 = \mathcal{V} - \mathbf{v}_{sw} \cdot \mathbf{n}$, being \mathbf{v}_{sw} the local mean speed of the solar wind, and the corresponding error, $d\mathcal{V}_0$. For the details, please, refer to Section 4.2.2 of Perrone et al. (2016). It is worth pointing out that $d\mathcal{V}_0$ is larger in the case of fast solar wind than in the slow wind case because is proportional to the value of the wind speed (the error on the solar wind velocity is estimated as the 5% of the value of the speed). Figure 16(a) shows \mathcal{V}_0 for the 33 structures, ordered by its increasing value, with the corresponding error bars. Contrary to what is found for the case of slow solar wind, in which the 25% of the observed structures had significant velocities different to zero (Perrone et al. 2016), in the present stream of fast solar wind all the structures are simply convected by the flow. Only a clear example of no convected structure is observed, but it is probably due to the incertitude in the identification of the range of localization. Moreover, also the distribution of \mathcal{V}_0 , normalised to the Alfvén speed, V_A (black solid line) and to the proton thermal speed, V_{th} (blue dot-dashed line) in panel (b) of Figure 16 suggests the same result, where the characteristic velocities are calculated in the upstream region for each structure, known from the sign of \mathcal{V}_0 . Both the distributions are peaked around 0 and vary between $[-1, 2]V_A$ or V_{th} . No fast structures are found, contrary to the case of slow solar wind (Perrone et al. 2016). Only an event of very fast structure ($\mathcal{V}_0 \sim 6V_A$) is observed, corresponding to the no convected structure in panel (a), that in any case does not have a statistical meaning.

6. CONCLUSIONS AND DISCUSSION

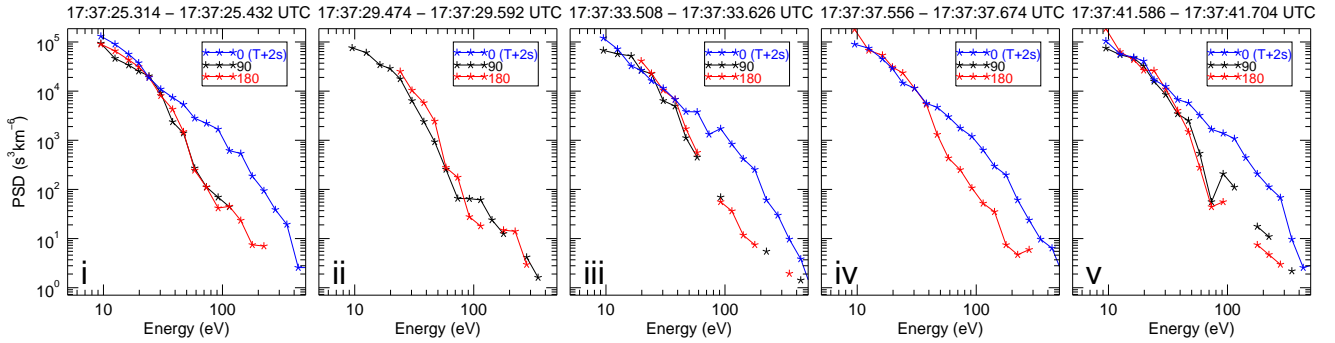


FIG. 14.— Five incomplete pitch angle distributions, taken during about 20 minutes surrounding the centre of the vortex chain in Figure 13. Each panel shows a cut of the electron distribution at pitch angles 0° (blue line), 90° (black line) and 180° (red line). The time of the cuts corresponds to the vertical green dot-dashed lines in Figure 13 for pitch angles 90° and 180° , while pitch angle 0° is taken 2 s later. No coverage of pitch angle 0° is available in panel ii, while in panel iv the same problem is found for pitch angle 90° .

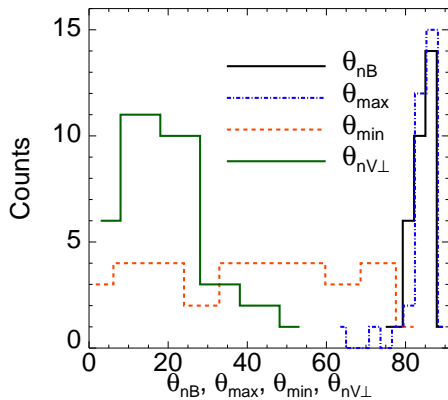


FIG. 15.— Distributions of the angles of the local magnetic field \mathbf{b}_0 with (i) the normal \mathbf{n} (θ_{nB} , black solid line); (ii) the direction of maximal variance \mathbf{e}_{\max} (θ_{\max} , blue dot-dashed line) and (iii) minimum variance \mathbf{e}_{\min} (θ_{\min} , red dashed line); and of the angle between \mathbf{n} and the local solar wind velocity in the (x, y) -plane of the BV -reference frame ($\theta_{nV\perp}$, green solid line).

In this paper, we have investigated the nature of magnetic turbulent fluctuations around ion scales in a stream of fast solar wind, by using high-resolution *Cluster* data. The results are complementary to the recent statistical study in slow wind plasma by Perrone et al. (2016).

The study of the distribution of energy in time and frequencies shows the presence of localized regions in time that cover a certain range of scale. The same non-homogeneous distribution of energy localized in time, covering certain frequencies, was already highlighted in slow solar wind (Perrone et al. 2016). Thus, independently of the streams, the solar wind ion scales appear to be characterized by a strong intermittency which could play an important role in dissipation and particle energization.

A detailed study of magnetic fluctuation in the range $f \in [0.1, 2]$ Hz has shown that this region is also characterized by a high phase coherence between the magnetic components and by a significant non-Gaussianity. The departure from Gaussianity of the turbulent fluctuations reflects a non-homogeneous (intermittent) distribution of the turbulent energy, with the appearance of structures characterized by a finite degree of phase syn-

chronization. Therefore, intermittency, phase coherence and non-Gaussian fluctuations are found to be strictly related, in agreement with previous studies (Koga et al. 2007; Lion et al. 2016).

We show that, at ion scales, the observed intermittency is related to convected coherent structures with a strong wave-vector anisotropy in the perpendicular direction with respect to the local magnetic field ($k_\perp \gg k_\parallel$). In particular, the fast solar wind appears to be dominated by Alfvén vortices (isolated or in chains), with small compressive part (for most of them the ratio between the parallel and the total magnetic energy is less than 10%), and by several current sheets aligned with the local magnetic field, convected by the flow. These results are in agreement with a recent analysis by Lion et al. (2016) in a stream of fast wind observed by *Wind* spacecraft. The authors found the presence of Alfvén vortex-like structures and current sheets, that drastically contributes to the spectral shape of the magnetic field spectrum at ion scales. Furthermore, the comparison of this stream of fast solar wind with the results described in Perrone et al. (2016) in slow wind context suggests that the latter one is much more complex, with the presence also of strongly compressive structures, such as magnetic holes, solitons and shocks, with smaller amplitudes with respect to the Alfvénic structures, but that propagate in the plasma rest frame.

In a separate study using the MSR technique, Roberts et al. (2017) studied intervals of fast and slow wind plasma. In the fast wind phase speeds were found to be very slow often below the Alfvén speed for incompressible and compressible magnetic fluctuations. Meanwhile in the slow wind the compressible magnetic field showed evidence of fast propagating fluctuations, with some faster than the magnetosonic speed. This is consistent with the results discussed in both Perrone et al. (2016) and in the present paper. Therefore, slow solar wind presents a more complex physics with respect to fast wind, where fast structures, moving in the flow, could lead to the generation of some instabilities with additional effects on particles (Papadopoulos 1972).

The difference in the observed families of structures in slow and fast streams fits also into a more general context of the source of these winds (Feldman et al. 2005). For example, the presence of compressive structures in slow solar wind could be the result of the in-

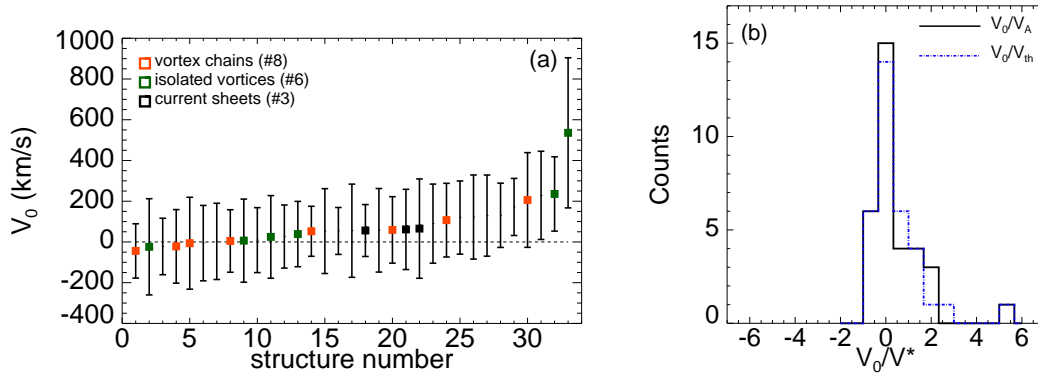


FIG. 16.— Panel (a): Velocity of 33 structures in the plasma rest frame, V_0 , with the corresponding error bars, arranged in increasing order of the V_0 values. The different kinds of the structures are indicated by different colours and the details can be found in the legend. Panel (b): Distribution of V_0 normalized to the Alfvén speed, V_A (black solid line) and to the proton thermal speed, V_{th} (blue dot-dashed line).

interaction of the wind with the heliospheric current sheet (Burlaga et al. 2002; Brooks et al. 2015) or be remnant features of large scale coronal structures (Wilcox & Ness 1967; McComas et al. 2000). Thanks to Solar Orbiter and Parker Solar Probe, it will be possible to measure the turbulent and structured electric and magnetic fields associated with shocks, reconnection and stochastic energization in unexplored plasma environments, investigating plasma physics in the source regions of both fast and slow wind. Moreover, Solar Orbiter and Parker Solar Probe will give access to the heliocentric variation of the turbulence, allowing the study electromagnetic field fluctuations and particle energization processes as a function of radial distance.

Understanding intermittency phenomenon and the related formation of small-scale coherent nonlinear structures could provide key insights into the general problem of dissipation in collisionless plasma and more particularly in solar wind. The physics of dissipation strongly depends on the different family of structures because of the different physical processes involved in the generation and/or evolution of the considered coherent structure. Our results (in the present paper for fast solar wind and in Perrone et al. (2016) for slow solar wind) show that the vortex-like structures are the dominant form in the observed structures; thus, they may play a major role in the dynamics of the solar wind plasma at ion scales. A very recent theoretical study in nearly incompressible magnetohydrodynamic (NI MHD) turbulence by Zank et al. (2017) has shown that two-dimensional vortex structures are explicitly predicted by the model. In particular the NI MHD formulation describes the transport of majority 2D, and minority slab, turbulence throughout the solar wind. This result supports the fact that in both fast and slow solar wind the vortex-like structures are the most frequent intermittent events. It is worth pointing out that the model for NI MHD turbulence deals with the fluid range while the present paper deals with coherent structures at kinetic scales. However, as far as coherent structures cover a very large range of scales, the detected strong events at ion scales show waveforms covering $\sim 30\rho_p$ (the diameter of the vortices). Therefore, the NI MHD turbulence model could

be still applicable.

The observed vortices can be divided in two sub-families with different properties. In particular, we found strongly localized vortices as well as vortex chains. In the first case, localized vortices could trap particles and, propagating in the flow, could excite density fluctuations and increase heat and mass transport processes. This is the scenario of a strong vortex turbulence (Aburjania et al. 2009). However, these isolated vortices could be the result of merging processes from smaller to larger scale structures, like as in the mechanism for self-organization in ideal fluids, creating a finite number of large, well separated vortices (Novikov & Sedov 1979; McWilliams 1984; Bracco et al. 2000). This phenomenon is called *vortex collapse* and one could expect similar phenomena to occur also in plasmas. For localized structures, as long as the mutual distance between the vortices is larger than their size, there is not interaction between them and they can be described as Alfvén-type vortices (Petviashvili & Pokhotelov 1992). However, when the vortices are closer together their shapes start to deform. The vortex merger is an example of interaction where the Alfvén vortex approximation is no longer valid (Schep et al. 1994). The main idea is that two aligned currents attract each other by the Lorentz force and can then coalesce. The generated vortex pattern has the characteristics of a collision of two vortices, and starts to deform the current distribution. Collisionless reconnection of the magnetic field takes place, changing the magnetic topology, and the magnetic flux is converted into electron momentum and ion vorticity, while the magnetic energy is transformed into electron energy (Kuvshinov et al. 1998; Bergmans & Schep 2001).

In the case of fast solar wind, we observed several examples of vortex chains where such interaction can take place, that could be related to a transient state of a collisionless reconnection. If it is the case, magnetic flux could be converted into electron momentum and ion vorticity, while the magnetic energy could be transformed into electron energy (Kuvshinov et al. 1998). Unfortunately, due to very scarce particle measurements at time resolutions comparable with their kinetic scales, the heating process and the complicated phase-space interaction

in turbulent solar wind still remain a puzzle. In particular, due to the low time resolution of the particle measurements on *Cluster*, there are not enough points within the structures to study the heating and/or the energization of the particles. Moreover, sometimes the low resolution can generate unphysical effects due to the procedure of data sampling and averaging (Perrone et al. 2014).

In March 2015, the Magnetospheric Multiscale (*MMS*) mission, with four identically instrumented spacecraft as *Cluster* but with a separation of ~ 10 km, has been launched. During Phase 2 of the mission, which started in February 2017, *MMS* apogee will be raised up to $25 R_E$ and it will spend times in solar wind. In particular, after September 2017 the apogee will be located on the day-side and many intervals of solar wind data will be indeed gathered. In this context, particle distribution functions will be measured with high time resolution (30 ms for electron distributions and 150 ms for ions) and more detailed information will be obtained to better understand the problem of dissipation in a such collisionless plasma.

However, although *MMS* has improved the temporal resolution for the particle measurements, angular/energy

resolution still remains insufficient to completely resolve solar wind ions. A key insight in the study of turbulence, energy dissipation and particle energization in the near-Earth environment might be provided by the Turbulence Heating ObservER (*THOR*) mission (Vaivads et al 2016), which is currently in the competitive study phase with two other missions at the ESA and it could be selected in end-2017. The main goal of this future space mission is to resolve kinetic scale processes, increasing angular and energy resolutions and the sensitivity of instruments, in particular for particle measurements.

ACKNOWLEDGMENTS

We thank the FGM, STAFF, CIS, WHISPER, EFW instrument teams and the ESA Cluster Science Archive. Moreover we thank PEACE team at MSSL for the electron data. D. P. would like to acknowledge A. Mangeney, S. Toledo Redondo, B. Lavraud, D. Burgess and the joint ESTEC/ESAC heliophysics group for helpful discussions. O. A. and M. M. thank CNES for the instrumental development of *Cluster*/STAFF and for the financial support. Authors would like to acknowledge the anonymous Referee for his/her comments, which helped to improve the manuscript.

APPENDIX

Multi-point Signal Resonator technique

In the present paper we show that the solar wind turbulence is strong with the presence of coherent structures, characterized by coherence (constant phase) over many scales. However, in the context of the solar wind turbulence, many studies have been performed by using the *k-filtering* technique which was developed for the analysis of multi-point magnetometer data from the Cluster mission (Pinçon & Lefeuvre 1991). The technique requires the assumptions of weak stationarity of the time series and that the signal can be described as a superposition of plane waves with random phases and a small component of isotropic noise. The Multi-point Signal Resonator (MSR) technique (Narita et al. 2011b) is an extension of the *k-filtering* technique and requires the same assumptions. The main difference is that the MSR technique uses an additional filter based on the MULTIPLE SIGNAL CLASSIFICATION (MUSIC) algorithm (Schmidt 1986), to improve the signal to noise ratio of the power spectrum in wave-vector space $P(\omega_{sc}, \mathbf{k})$. This method has also been validated for a synthetic signal which consists of random phase plane waves and non-random coherent structures (Roberts et al. 2014). Moreover, Roberts et al. (2014) showed that the presence of coherent components in the signal did not affect the recovery of any incoherent components. Using this approach the wave-number k with the maximum power in the signal at a given spacecraft frequency ω_{sc} can be obtained without the need of Taylor's hypothesis. Moreover, the plasma frame frequency and the phase speed of the fluctuations can be obtained by Doppler shifting to the plasma frame according to the equations $\omega_{pla} = \omega_{sc} - \mathbf{k} \cdot \mathbf{v}_{sw}$ and $v_{ph} = \omega_{pla}/k$.

To verify the applicability of the MSR technique on a stream characterized by the presence of coherent structures, where its assumptions are seemingly in contradiction with the idea of strong turbulence, we perform the MSR analysis on this interval of fast solar wind, in two different ways combining data from the four spacecraft. The first is on the three components of the magnetic field which is dominated by incompressive fluctuations. The second method will focus only on the compressive fluctuations δB_{\parallel} of the magnetic field by using a single input (the magnitude of the magnetic field) at each spacecraft. The application of the method to a single time series at each craft is discussed in detail by Roberts et al. (2017).

It is worth pointing out that this technique has some limitations. First of all, the fluctuations which can be surveyed are limited to scales comparable to the size of the Cluster tetrahedron. The maximum wave-number is given by the relation $k_{max} = \pi/d$ where d is the mean spacecraft separation (Sahraoui et al. 2010; Roberts et al. 2014). Additionally the tetrahedron needs to be close to regular such that the spacecraft sample homogeneously in space. In this case planarity and elongation parameters (Robert et al. 1998) are low $P \sim E \lesssim 0.15$, indicating that the geometry is close to that of a regular tetrahedron. Moreover, there are two sources of error for the plasma frame speed of the fluctuations. The first one consists in the error on determining the solar wind velocity which dominates the estimation of the plasma frame frequency ω_{pla} , which is assumed to be 10% (Martz et al. 1993). The second source of error is on the determination of the wave-number from the method. Sahraoui et al. (2010) demonstrated that for a plane wave the wave-number is identified with a relative error of 10% at a wave-number of $k_{max}/25$, that decreases quickly to 1% at k_{max} . Furthermore, using the same approach when only a single time series is used at each spacecraft (as is the case when using the $|B|$ as an input) the errors in determining the wave-vector are similar (Roberts et al. 2017).

The results of this analysis, for the considered interval of fast solar wind, are presented in Figure 17, where panels (a), (c) and (e) show the results when applied to the total magnetic fluctuations, while panels (b), (d) and (f) when

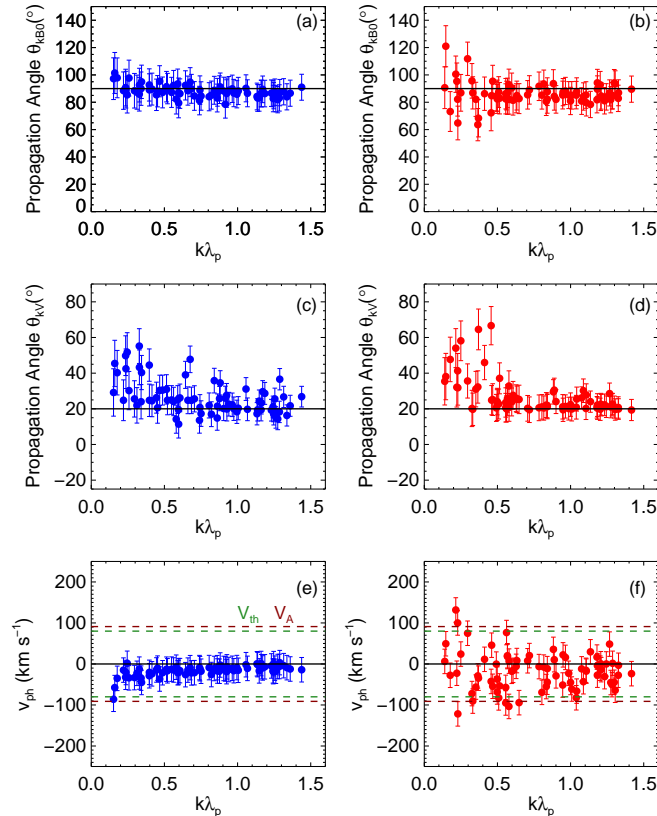


FIG. 17.— Results from the k -filtering analysis for total (left panel, blue color) and compressive (right panel, red color) magnetic fluctuations. Panels (a) and (b): propagation angles with respect to the global magnetic field direction, θ_{kB_0} . Horizontal black solid lines indicate $\theta_{kB_0} = 90^\circ$. Panels (c) and (d): propagation angles with respect to the global velocity field direction. Horizontal black solid lines indicate $\theta_{kV} = 20^\circ$. Panels (e) and (f): phase speeds of the fluctuations. Horizontal black solid lines indicate $V_{ph} = 0$ km/s, while the Alfvén speed (horizontal dark purple dashed lines) and the proton thermal speed (horizontal green dashed lines) are given as references.

it is applied to the fluctuations in the magnitude. It is worth pointing out that, unlike the timing method where each event is individually analyzed, the MSR technique has a global vision of the whole interval. This would not only include coherent structures but could also contain power from other sources such as incoherent plasma waves. At each frequency the wavevector corresponding to the most energetic fluctuations is recovered; therefore, it is possible that the MSR method gives results exactly for the coherent structures in the paper, but we cannot rule out contributions from other sources. Indeed, the MSR technique shows results similar to the timing method. Both total and compressive fluctuations are characterized by a small phase speed ($v_{ph} < V_A, V_{th}$) and propagation angles almost perpendicular to the global magnetic field ($\theta_{kB_0} \sim 90^\circ$), with $\theta_{kV} \sim 25^\circ$, even if for the compressive fluctuations a larger spread in both these values is observed. Nevertheless, the fact that k is quasi-aligned with the solar wind speed could be an effect of the sampling direction. Therefore, it is not possible to conclude on the (non)gyrotropy of the turbulent fluctuations, because no information of the k perpendicular to the solar wind velocity are known. A numerical study to test this point is needed and it will be the subject for a future work.

The results of the MSR technique on the phase speed and propagation angle are consistent with previous case (Sahraoui et al. 2010; Roberts et al. 2013) and statistical studies (Roberts et al. 2015; Perschke et al. 2016) in the solar wind. This has variously been interpreted as evidence of quasi-linear waves that propagate slowly in the plasma frame (such as the quasi-perpendicular Kinetic Alfvén Wave (Sahraoui et al. 2010)) or coherent structures with $k_\perp \gg k_\parallel$ which are advected by the plasma bulk flow or a combination of these two phenomena (Roberts et al. 2013, 2015). However, in the present work, by looking directly at the magnetic fluctuations around ion scales in the region of high intermittency, it has been clearly shown that the considered time interval is covered by coherent structures (making up $\sim 30\%$ of the interval). These intermittent structures are characterized by a perpendicular wave-vector anisotropy (see the distribution of θ_{nB} in Figure 15) and small velocities of propagation in the plasma frame (see Figure 16). Generally structures which have very weak compressibility such as current sheets and vortices are advected with the flow. Meanwhile some compressive vortices are measured by the timing method to have higher speed and could account for the larger spread of values seen here.

REFERENCES

- Aburjania, G. D., Chargazia, Kh. Z., Zelenyi, L. M., & Zimbaro, G. 2009, *Nonlinear Proc. in Geophys.*, 16, 11
- Alexandrova, O., Mangeney, A., Maksimovic, M., Cornilleau-Wehrin, N., Bosqued, J.-M. & André, M. 2006, *J. Geophys. Res.*, 111, A12208

- Alexandrova, O., Carbone, V., Veltri, P., & Sorriso-Valvo, L. 2007, *Planet. Spa. Sci.*, 55, 2224
- Alexandrova, O. 2008, *Nonlin. Processes Geophys.*, 15, 95
- Alexandrova, O., Carbone, V., Veltri, P., & Sorriso-Valvo, L. 2008, *Astrophys. J.*, 674, 1153
- Alexandrova, O., & Saur, J. 2008, *Geophys. Res. Lett.*, 35, 15102
- Alexandrova, O., Saur, J., Lacombe, C., Mangeney, A., Mitchell, J., Schwartz, S. J., & Robert, P. 2009, *Phys. Rev. Lett.*, 103, 165003
- Alexandrova, O., Lacombe, C., Mangeney, A., Grappin, R., & Maksimovic, M. 2012 *Astrophys. J.*, 760, 121
- Bale, S. D., Kellogg, P. J., Mozer, F. S., Horbury, T. S., & Reme, H. 2005, *Phys. Rev. Lett.*, 94, 215002
- Balogh, A., Carr, C. M., Acuña, M. H., Dunlop, M. W., Beek, T. J., Brown, P., Fornacon, K.-H., Georgescu, E., Glassmeier, K.-H., Harris, J., Musmann, G., Oddy, T., & Schwingenschuh, K. 2001, *Ann. Geophys.*, 19, 1207
- Bergmans, J., & Schep, T. J., *Phys. Rev. Lett.*, 87, 19
- Boldyrev, S., Horaites, K., Xia, Q., & Perez, J. C. 2013, *Astrophys. J.*, 777, 41
- Bourouaine, S., Alexandrova, O., Marsch, E., & Maksimovic, M. 2012, *Astrophys. J.*, 749, 102
- Bracco, A., McWilliams, J. C., Murante, G., Provenzale, A., & Weiss, J. B. 2000, *Phys. Fluids*, 12, 2931
- Brooks, D. H., Ugarte-Urra, I., & Warren, H. P. 2015 *Nature Comm.*, 6, 5947
- Bruno, R., Carbone, V., Veltri, P., Pietropaolo, E., & Bavassano, B. 2001 *Planet. Spa. Sci.*, 49, 1201
- Bruno, R., & Carbone, V. 2013, *Living Rev. Solar Phys.*, 10, 2
- Bruno, R., Trenchi, L., & Telloni, D. 2014, *Astrophys. J. Lett.*, 793, L15
- Burlaga, L. F., Ness, N. F., Wang, Y.-M., & Sheeley, N. R. 2002, *J. Geophys. Res.*, 107, 20
- Chen, C. H. K., Mallet, A., Yousef, T. A., Schekochihin, A. A., & Horbury, T. S. 2011, *Mon. Not. R. Astron. Soc.*, 415, 3219
- Cornilleau-Wehrlin, N., Chanteur, G., Perraut, S., *et al.* 2003, *Ann. Geophys.*, 21, 437
- Décraeu, P. M., Ferreau, P., & Krasnoselskikh, V. 2001, *Ann. Geophys.*, 19, 1241
- Dunlop, M. W., Southwood, D. J., Glassmeier, K.-H., & Neubauer, F. M. 1988, *Adv. Space Res.*, 8, 273
- Dunlop, M. W., Balogh, A., Glassmeier, K.-H., & Robert, P. 2002, *J. Geophys. Res.*, 107, 1384
- Farge, M. 1992, *Annual Rev. Fluid Mech.*, 24, 395
- Fazakerley, A. N., Lahiff, A. D., Wilson, R. J., Rozum, I., Anekallu, C., West, M., & Bacai, H. 2009, *PEACE Data in Cluster Active Archive in The Cluster Active Archive* (pp. 129–144). Springer
- Feldman, U., Landi, E., & Schwadron, N. A. 2005, *J. Geophys. Res.*, 110, A07109
- Frisch, U. 1995, *Turbulence: The legacy of A. N. Kolmogorov* Cambridge: Cambridge Univ. Press
- Gary, S. P. 1986, *J. Plasma Phys.*, 35, 431
- Goldstein, M. L., Roberts, D. A., & Fitch, C. A. 1994, *J. Geophys. Res.*, 99, 11519
- Greco, A., Matthaeus, W. H., D'Amicis, R., Servidio, S., & Dmitruk, P. 2012a, *Astrophys. J.*, 749, 105
- Greco, A., & Perri, S. 2014, *Astrophys. J.*, 784, 163
- Greco, A., Perri, S., Servidio, S., Yordanova, E., & Veltri, P. 2016, *Astrophys. J. Lett.*, 823, L39
- Grinsted, A., Moore, J. C., & Jevrejeva, S. 2004, *Nonlinear Proc. in Geophys.*, 11, 561
- Gustafsson, G., Bostrom, R., Holback, B., *et al.* 1997, *Space Sci. Rev.* 79, 137
- Hamilton, K., Smith, C. W., Vasquez, B. J., & Leamon, R. L. 2008, *J. Geophys. Res.*, 113, A01106
- Harris, E. G. 1961, *Il Nuovo Cimento*, 2, 115
- He, J., Marsch, E., Tu, C., Yao, S., & Tian, H. 2011, *Astrophys. J.*, 731, 85
- He, J., Tu, C., Marsch, E., & Yao, S. 2012, *Astrophys. J. Lett.*, 745, L8
- Johnstone, A. D., Alsop, C., Burge, S. *et al.* 1997, *Space Sci. Rev.* 79, 351
- Kiyani, K. H., Chapman, S. C., Sahraoui, F., Hnat, B., Fauvarque, O., & Khotyaintsev, Yu. V. 2013, *Astrophys. J.*, 763, 10
- Koga, D., Chian, A. C.-L., Miranda, R. A., & Rempel, E. L. 2007, *Phys. Rev. E*, 75, 046401
- Kolmogorov, A. N. 1941, *Dokl. Akad. Nauk SSSR*, 30, 301
- Kuvshinov, B. N., Lakhin, V. P., Pegoraro, F., & Schep, T. J. 1998, *J. Plasma Phys.*, 59, 727
- Lacombe, C., Alexandrova, O., & Matteini, L. 2017, *Astrophys. J.*, in press
- Leamon, R. J., Smith, C. W., Ness, N. F., Matthaeus, W. H., & Wong, H. K. 1998, *J. Geophys. Res.*, 103, 4775
- Leamon, R. J., Matthaeus, W. H., Smith, C. W., Zank, G. P., Mullan, D. J., & Oughton, S. 2000, *Astrophys. J.*, 537, 1054
- Lion, S., Alexandrova, O., & Zaslavsky, A. 2016, *Astrophys. J.*, 824, 47
- Martz, C., Sauvand, J. A., & Rème, H. 1993 Accuracy on Ion Distribution measurements and related parameters using the Cluster CIS Experiment in *Spatio-Temporal Analysis for Resolving Plasma Turbulence (START)*
- Matthaeus, W. H., Servidio, S., Dmitruk, P., Carbone, V., Oughton, S., Wan, M., & Osman, K. T. 2012, *Astrophys. J.*, 750, 103
- McComas, D. J., Barraclough, B. L., Funsten, H. O., & *et al.* 2000, *J. Geophys. Res.*, 105, 10419
- McWilliams, J. C. 1984, *J. Fluid Mech.*, 146, 21
- Narita, Y., Glassmeier, J.-H., & Motschmann, U. 2011a, *Ann. Geophys.*, 29, 351
- Narita, Y., Gary, S. P., Saito, S., Glassmeier, J.-H., & Motschmann, U. 2011b, *Geophys. Res. Lett.* 38, L05101
- Novikov, E. A., & Sedov, Yu. B. 1979 *Soviet Phys. JETP* 50, 297
- Papadopoulos, K. 1972, *Astrophys. J.*, 179, 931
- Pedersen, A. 1995, *Ann. Geophys.* 13, 118
- Pedersen, A., Décréau, P., Escoubet, C.-P., Gustafsson, G., Laakso, H., Lindqvist, P.-A., Lybakk, B., Masson, A., Mozer, F., & Vaivads, A. 2001, *Ann. Geophys.* 19, 1483
- Perri, S., Goldstein, M. L., Dorelli, J. C., & Sahraoui, F. 2012, *Phys. Rev. Lett.* 109, 191101
- Perrone, D., Bourouaine, S., Valentini, F., Marsch, E., & Veltri, P. 2014b, *J. Geophys. Res.* 119, 2400
- Perrone, D., Alexandrova, O., Mangeney, A., Maksimovic, M., Lacombe, C., Rakoto, V., Kasper, J. C., & Jovanovic, D. 2016, *Astrophys. J.*, 826, 196
- Perschke, C., Narita, Y., Motschmann, U., & Glassmeier, K. H. 2016, *Phys. Rev. Lett.*, 116, 125101
- Petviashvili, V. I., & Pokhotelov, O. 1992, *Solitary Waves in Plasmas and in the Atmosphere* (Gordon & Breach Science Pub)
- Pinçon, J.-L., & Lefeuvre, F. 1991, *J. Geophys. Res.*, 96, 1789
- Rème, H., Aoustin, C., Bosqued, J. M. *et al.* 2001, *Ann. Geophys.*, 19, 1303
- Robert, P., Roux, A., Harvey, C. *et al.* 1998, *Tetrahedron Geometric Factors, in Analysis Methods for Multi-Spacecraft Data*, ISSI Sci. Rep., ESA Publ. Div., Noordwijk, Netherlands
- Roberts, O. W., Li, X., & Li, B. 2013, *Astrophys. J.*, 769, 58
- Roberts, O. W., Li, X., & Jeska, L. 2014, *Geosci. Instrum. Method. Data Syst.*, 3, 247
- Roberts, O. W., Li, X., & Jeska, L. 2015, *Astrophys. J.*, 802, 2
- Roberts, O. W., Li, X., Alexandrova, O., & Li, B. 2016, *J. Geophys. Res.*, 121, 3870
- Roberts, O. W., Narita, Y., Li, X., Escoubet, C. P., & Laakso, H. 2017, *J. Geophys. Res.*, 122, 6940
- Sahraoui, F., Goldstein, M. L., Belmont, G., Canu, P., & Rezeau, L. 2010, *Phys. Rev. Lett.*, 105, 131101
- Sahraoui, F., Huang, S. Y., Belmont, G., Goldstein, M. L., Retinò, A., Robert, P., & De Patoul, J. 2013, *Astrophys. J.*, 777, 15
- Salem, C., Mangeney, A., Bale, S. D., & Veltri, P. 2009, *Astrophys. J.*, 702, 537
- Salem, C. S., Howes, G. G., Sundkvist, D., Bale, S. D., Chaston, C. C., Chen, C. H. K., & Mozer, F. S. 2012, *Astrophys. J. Lett.*, 745, L9
- Schmidt, R. O. 1986 *IEEE Transitions on Antennas and Propagation* 34, 276
- Schep, T. J., Pegoraro, F., & Kuvshinov, B. N. 1994, *Phys. Plasmas* 1, 9
- Schwartz, S. J. 1998, Shock and discontinuity normals, Mach numbers, and related parameters, in *Analysis Methods for Multi-Spacecraft Data*, ISSI Sci. Rep., ESA Publ. Div., Noordwijk, Netherlands
- She, Z.-S., Jackson, E., & Orszag, S. A. 1990, *Nature*, 344, 226

- Smith, C. W., Hamilton, K., & Vasquez, B. J. 2006, *Astrophys. J. Lett.*, 645, L85
- Telloni, D., Bruno, R., & Trenchi, L. 2015, *Astrophys. J.*, 805, 1
- TenBarge, J. M., Podesta, J. J., Klein, K. G., & Howes, G. G. 2012, *Astrophys. J.*, 753, 107
- Torrence, C., & Compo, G. P. 1998, *Bull. Am. Meteorol. Soc.*, 79, 61
- Vaivads, A., Retinò, A., Soucek, J., *et al.* 2016 *J. Plasma Phys.* 82, 905820501
- Veltri, P., & Mangeney, A. 1999, in *AIP Conf. Proc.* 471, *Solar Wind IX* ed. S. Habbal (USA), 543
- Veltri, P. 1999, *Plasma Phys. Control. Fusion*, 41, A787
- Widrow, B., & Kollár, I. 2008, *Spectrum of Quantization Noise and Conditions of Whiteness in Quantization Noise: Roundoff Error in Digital Computation, Signal Processing, Control, and Communications* (pp. 529–562). Cambridge University Press
- Wilcox, J. M., & Ness, N. F. 1967, *Solar Phys.*, 1, 437
- Wu, P., Perri, S., Osman, K., Wan, M., Matthaeus, W. H., Shay, M. A., Goldstein, M. L., Karimabadi, H., & Chapman, S. 2013 *Astrophys. J. Lett.*, 763, L30
- Zank, G. P., Adhikari, L., Hunana, P., Shiota, D., Bruno, R., & Telloni, D. 2017 *Astrophys. J.*, 835, 147